Thesis for the degree of Licentiate of Engineering

Modeling stormwater transport through unsaturated green roof substrates

Kaj Pettersson

Department of Architecture and Civil Engineering
Division of Building Technology
CHALMERS UNIVERSITY OF TECHNOLOGY
Göteborg, Sweden 2018

Modeling stormwater transport through unsaturated green roof substrates
Kaj Pettersson

Licentiatavhandlingar vid Chalmers tekniska högskola

Department of Architecture and Civil Engineering
Chalmers University of Technology
SE–412 96 Göteborg, Sweden
Telephone + 46 (0) 31 – 772 1000

Cover: Water infiltration of a randomly packed bed, see Figure 3.4 on page 27.

Typeset by the author using LaTeX.

Printed by Chalmers Reproservice
Göteborg, Sweden 2018

Abstract

In recent decades there has been an increase in research regarding green roofs and similar technologies. This increased interest is driven by the requirements of urban development and its effects both on humans and the environment. Additionally, the predicted increase in weather severity in the future is raising concerns on the capabilities of urban environments and their stormwater management systems to cope with the increase.

Green roofs can be used as a space-conscious solution for improving stormwater management in urban areas as well as contributing to, for example, building protection and pollution and noise reduction. In order to fully utilize them effectively for stormwater runoff reduction it is necessary to quantify their effect and optimize their performance in a given climate. This optimization can take the form of placement on structures or by design within the green roof construction itself.

This work focuses on optimization of design by applying computational fluid dynamics and lattice Boltzmann theory to the soil growth substrate. Computational fluid dynamics is used for modeling the flow through the green roof growth substrate (soil layer) at the macrososcopic scale while a lattice Boltzmann model is applied to the mesoscopic (soil particle) scale. Using these methods, the efficacy at water retention and drainage of given soil particles and full-sized green roofs can be determined. This work covers the framework covering both scales however the methodology is applied only to the mesoscopic scale.

The focus within the mesoscopic scale is primarily on the hydrophilicity of the particles in the soil and its impact on liquid imbibition. Also included is an exploration on the liquid-air interfacial area and liquid penetration depth to aid in the analysis of the results. The findings of the study suggest particle hydrophilicity plays an important role in the imbibition process, particularly under light to medium rainfall conditions. In addition a pore blocking phenomenon is identified which requires further analysis. Finally, plans for future work and the closure of the two-framework methodology proposed in this work is discussed.

Keywords: Green roofs, modeling, CFD, Lattice Boltzmann, porous media, multiphase, saturation.

Acknowledgments

Firstly I would like to thank my supervisors, particularly Angela and Pär for their support and feedback and also for the freedom I am given in how I approach the challenges within my research. In addition I would like to thank Dario for his guidance and assistance in learning the lattice Boltzmann method as well as allowing me the use of his code! I would also like to thank Srdjan for his input and ideas as without his suggestion of applying lattice Boltzmann. Additionally, I would like to mention my colleagues and friends who get to listen to me ramble on and to double check my logic and occasionally code. Two minds are always better than one when it comes to finding a misplaced ;!

I would also like to thank my funding providers for their contributions to my research.

Last but certainly not least I thank my family who have always cheered me on.

Kaj Pettersson
Göteborg, December 2018

List of Publications

This thesis is based on the following appended papers:

Paper 1. Kaj Pettersson, Sinisa Krajnovic, Angela Sasic Kalagasidis and Pär Johansson. *Simulating wind-driven rain on buildings facades using Eulerian multiphase with rain phase turbulence model.* Building and Environment 106 (2016), pp. 1–9..

Nomenclature

$\mathscr{A}_{r_1 r_2}$	–	Lattice particle scattering matrix
A_{ls}	–	Liquid-solid interfacial area
$\mathbf{B}$	–	Arbitrary solution matrix to boundary value problem
$\mathbf{b}$	–	Arbitrary solution matrix to boundary value problem
$\mathscr{C}$	–	Boltzmann collision operator
C_{vm}	–	Pore-scale flow inhomogeneity virtual mass empirical coefficient
$\vec{c}_r$	–	Lattice node connection vectors
c_s	–	Speed of sound coefficient
d	–	Particle diameter
d_{eff}	–	Particle effective diameter
e	–	Particle conversion coefficient
$\vec{F}$	–	External force term
f	–	Probability density function
f^e	–	Equilibrium probability density function
$\hat{f}$	–	Post-collision probability density function
$\mathbf{g}$	–	Gravity vector
g	–	Gravity scalar
$\vec{g}$	–	Relative velocity between particles
h	–	Rainfall depth characteristic length
h_c	–	Liquid penetration depth along the main flow direction
$\mathbf{I}$	–	Identity matrix
I	–	Particle collision differential cross-section
$\mathbf{K}$	–	Scalar-valued permeability
$\mathbf{K}$	–	Permeability tensor
$k_{r\omega}$	–	Relative permeability
L	–	LBM domain characteristic length
L_p	–	Pipe length
L_0	–	Macroscopic characteristic length
l_{cap}	–	Porous medium capillary radius
$l_{\Delta P}$	–	Liquid volume thickness
M	–	Particle mass
m	–	van Genuchten fitting coefficient
$\dot{m}_{\omega\eta}$	–	Interphasic mass transfer
$\mathbf{n}$	–	Outward normal
$\mathbf{n}_{ls}$	–	Liquid-solid interface outward normal
N	–	number of particles

n – van Genuchten fitting coefficient
n_r – Lattice occupancy number
$\tilde{n}_r$ – Post-collision lattice occupancy number
$\vec{p}$ – Phase space momenta
p_a – Air phase pressure
p_c – Capillary pressure
p_g – Pressure scaling value
p_l – Liquid phase pressure
$\tilde{p}_l$ – Liquid phase pressure spatial deviation
q – van Genuchten closure model fitting coefficient
R_c – Capillary radius
R_r – Spatial and temportal probability density function total fluctuations
r – Lattice node number
r_{eff} – Effective pore radius
r_r – Spatial and temportal probability density function fluctuations
r_0 – Averaging volume characteristic length
$\mathscr{S}$ – Boltzmann streaming operator
S_e – Effective saturation
S_l – Saturation
$S_{\alpha,\omega}$ – Phasic source term
t – Time
t^* – Dimensionless time
$\mathbf{u}_l$ – Liquid phase free-flow velocity
$\mathbf{u}_{l,int}$ – Liquid phase interfacial velocity
$\mathbf{u}_{l,\infty}$ – Liquid phase free-flow velocity
U – Velocity
$\overline{U}$ – Spatially averaged velocity
$\mathbf{v}_l$ – Liquid phase Darcy velocity
$\tilde{\mathbf{v}}_l$ – Liquid phase velocity spatial deviation
V – Total averaging volume
V_l – Liquid phase volume
$\vec{v}$ – Phase space velocity
w – Cementation coefficient
$\vec{x}$ – Phase space positional coordinates
α^* – Dimensionless slip coefficient
α_ω – Phase volume fraction
β_1 – Dimensionless jump condition coefficient
β_2 – Dimensionless jump condition coefficient
Γ_ω – Phasic diffusion coefficient
γ – Liquid-air surface tension
ϵ – Porosity
η – Phase indicatior variable, can be liquid and air
θ – Volumetric water content
θ_c – Liquid-air contact angle
θ_r – Residual volumetric water content
θ_s – Saturated volumetric water content

κ	–	Hydraulic conductivity
κ_r	–	Equivalent relative hydraulic conductivity
κ_s	–	Saturated hydraulic conductivity
μ_l	–	Liquid phase dynamic viscosity
$\mu_{l,eff}$	–	Liquid phase effective dynamic viscosity
ν_a	–	Air phase kinematic viscosity
ν_l	–	Liquid phase kinematic viscosity
ρ_a	–	Air phase density
ρ_l	–	Liquid phase density
ρ_{wall}	–	Contact angle equivalency in LBM code
τ	–	Arbitrary Darcy's law unsteady term coefficient
τ_{en}	–	Volume-averaged energy equation Darcy's law unsteady term coefficient
τ_f	–	Relaxation time coefficient
τ_{va}	–	Volume-averaged Darcy's law unsteady term coefficient
τ_{vm}	–	Virtual mass Darcy's law unsteady term coefficient
ϕ_ω	–	Arbitrary scalar quantity
ψ_l	–	Liquid phase scalar or vector value
Ω	–	Particle collision characteristic angle
ω	–	Phase indicatior variable, can be liquid and air
Bo	–	Bond number
Re	–	Reynolds number

Contents

Part I

Summary

Chapter 1

Introduction

This text concerns the modeling of stormwater as it passes through an unsaturated porous medium, however before delving into the details it is logical to provide some background information on the topics involved as well as motivate *why* this research is undertaken at all. With this in mind we will begin with a discussion on green roofs (our porous medium of choice) and why we wish to model stormwater flowing through them. This discussion will be followed by a short explanation on the primary technique involved in modeling such problems, computational fluid dynamics.

1.1 An introduction to green roofs

Green roofs can be characterized as any roof construction incorporating vegetation which can range from moss, sedum and grasses to bushes and trees. Their use stretches back to medieval times at the very latest and excavations have shown their implemetation in various parts of the world. Perhaps most famously they were used by the Viking settlers in Newfoundland and Iceland around 700-1000 A.D. In more modern times these types of roofs have experienced a resurgence of interest within the building sector for a variety of reasons, however the designs employed today are slightly different in terms of layering and materials. Most green roofs consist of several layers, as shown in Figure 1.1.

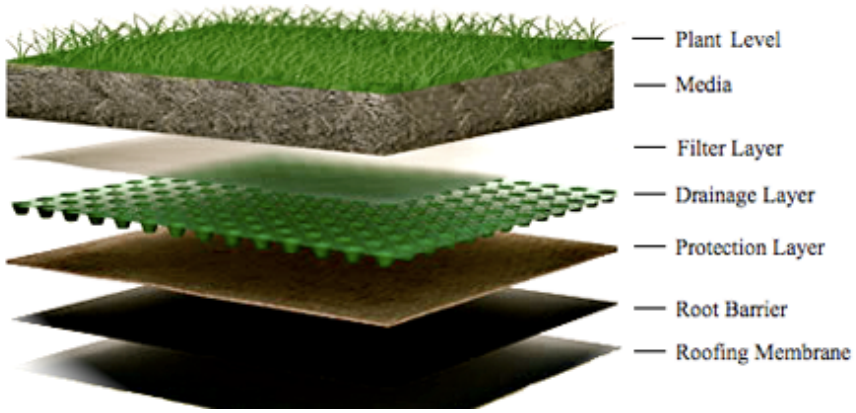

Figure 1.1: Green roof layering, image courtesy of Godfrey Roofing Inc. [1].

There must be a base roofing membrane layer that protects the interior of the structure in case of any leakage. Above this is a root barrier to prevent any infiltration of plant material into the primary structure. This is particularly important if grasses and trees are used due to their extensive root systems. Above this sits a drainage element that may consist of a cup structure as shown above or other drainage material such as lightweight expanded clay aggregate (LECA). This layer is primarily meant to facilitate removal of excess water from the roof once it passes through the vegetation and growth substrate layers. Above this drainage layer sits a filter fabric or similar material to prevent soil and other particulates from clogging the drainage layer and causing extraneous maintanence. The final layers are the plant and, of particular interest, the growth media (or substrate). The growth substrate may consist of a large variety of materials, from peat moss, to gravel and clay, etc. It is essentially soil though the exact composition varies on the vegetation and sourcing by production companies. It is this layer that we wish to look at more closely as it plays a critical role in a green roof's ability to capture stormwater and retain it. This process is important for two reasons; one being that the roof should retain sufficient moisture to provide for the vegetations' continued survival, the other being that it releases water so that the roof suffers no damage and the vegetation is not flooded.

The primary benefits of green roofs can be defined into a few categories.

- Aesthetic effects and their contribution to social wellbeing.
- Pollution and noise reduction and urban habitat creation.
- Contribution to urban stormwater management, climate control within the structure and building facade protection.

It is understandably difficult to quantify the social well-being benefits of green roofs or similar constructions so we will focus on the measurable impacts and studies. There has been research into the ability of green roofs to remove particulate as well as heavy metal pollution from the urban environment. One such study involved to usage of seaweed in the growth medium to trap heavy metals such as Cadmium, Nickel, and Chromium and the findings suggested viability of such an inclusion [2]. Another such example is the investigation on the acoustic efficiency of a green wall with the results ranging from 0-10dB reductions depending on frequency and height level [3].

Of these benefits, stormwater runoff reduction is the most documented. Historically the motivation for this is the increase in rainfall [4] and the subsequent interest in using green roofs to minimize flooding occurances. This work has been undertaken on a global scale, such as Great Britain [5], Italy [6] and Hong Kong [7], to name a few. The research into stormwater runoff reduction consists of two practical approaches. The first approach one can take is: *how can we optimize green roofs by placement?* This question is difficult to answer in practice and we will cover a few of the reasons why. In order to optimize placement of green roofs in an urban environment we must have some data on a number of items. Firstly we must know where on a

building the rain falls most, which is immensely difficult to predict. Predicting rainfall patterns on a building facade has been researched quite actively through the application of computational fluid dynamics as well as collecting experimental data. Blocken and Carmeliet have utilized CFD to predict rainfall on building facades by extending steady-state solution methods to transient systems [8], [9]. Inclusion of additional terms such as turbulent dispersion [10], [11] and incident wind directions [12] (oblique) have improved the accuracy of the approach and its applicability. Experimental data for use in validating such results has been collected in a few locations including at VLIET in Belgium [13], EMPA in Switzerland [14] and Norway [15]. The details of approach can be found in the references above. The author expanded upon the methodology applied in these papers by including a turbulence model directly to solve for turbulent dispersion in the entire domain however the results were mixed due to numerical instabilities and spatial averaging difficulties [16].

The difficulties involved in predicting rainfall patterns on structures stems from highly variable wind directions, rainfall intensities and the urban morphology itself. More damagingly than these modeling impracticalities are the restrictions placed on spatial and temporal resolution imposed by using the modeling techniques themselves, although these are sometimes ignored to the detriment of result accuracy. Thus without significant advances in techniques or computational power it is difficult to champion this alternative for optimization, particularly at such scales as urban districts. This leaves us with another option by which we can attempt to improve urban stormwater management, *optimization by design.*

1.2 Aim of the research

The reasoning of optimization by design leads us to the following conclusions when taking the structure of a green roof into account. One cannot easily isolate and quantify the contributions of the vegetation on stormwater retention, though many researchers such as [17] and [18] are working on this issue. The drainage layer design can be optimized for given rainfall intensities but this layer does not have the capacity for absorption and so we can quite easily estimate its performance. The most logical layer to focus on for improvement is the growth substrate, where we have definite flexibility on material choice and how we mix and layer it. Thus we must either perform extensive experiments for each possibility or apply some theoretical framework and methodology to aid us in this endeavor, enter computational fluid dynamics (CFD). CFD has been chosen because it is a powerful tool for accurately modeling flows of most liquids (including gases) with great accuracy. It is dissimilar to empirical approaches because the solutions are not tuned from experimentation, thus the method can be applied to inummerable cases with ease while maintaining confidence in the results. In addition, the method has been extensively validated against experimental results and is a perfect candidate of choice for our problem.

1.3 A brief explanation of computational fluid dynamics

Computational fluid dynamics (CFD) is a numerical methodology for solving the equations of fluid flow, most notably the Navier-Stokes equations. It was first developed in the 1920's and progressed in complexity and scope over the century. It is now used to model a large variety of problems in engineering and other scientific and artistic fields. The applications within engineering range from the microscopic to the macroscopic scale. Examples range from tracking the motion of a single microscopic particle in a given flow to airflow and turbulent effects around cars or trains. In many cases it is necessary to look at the problem on many levels of detail and gain an understanding of the most important processes at work in a particular problem. This can be the effect of gravity, particles bouncing off one another, the speed of the flow, density and viscosity of the fluid, and so on. It is a very powerful technique for reaching the desired level of accuracy in a solution to a particular problem for the lowest computational and time cost. The downsides of the method are mainly difficulties in correctly defining the problem and constructing the appropriate computational grid to accurately capture the physics involved. In general these computations are quite expensive in terms of computational power and the time required to solve the problem accurately, ranging from hours to months depending upon the problem complexity.

1.4 Document structure

The application of this technique, in particular to a problem as complex as the one we propose, requires a thorough background in the theoretical framework with which we will work and its complimentary limitations, outside of which the framework no longer applies. We begin constructing this framework by deriving the governing equations for subsurface flow and work in Chapter 2 and conclude with the theory behind the Lattice Boltzmann method in Chapter 3. The following chapters discuss the implementation of the technique and the results generated by its application, and finally a look into future work.

Chapter 2

Macroscale simulations using CFD

In this chapter we introduce the theoretical framework required to calculate subsurface flow. A thorough derivation of the relevant equations is undertaken with the aim of providing the reader with a solid background for the limitations and assumptions of the model. If we ignore these limitations and assumptions we run the risk of creating a framework that is mathematically and physically inconsistent and its application to unsuitable problems can lead to inaccurate and ultimately irrelevant results. The information provided by the derivation is invaluable when discussing the application of this framework to our problem, particularly when we reach the transient multiphase extensions that are necessary to describe stormwater flow through a green roof substrate.

2.1 Deriving Darcy's law for single phase flow

The derivation of the subsurface flow equation, known as Darcy's law, begins from the Stokes equation for steady, single phase incompressible flow

$$\nabla \cdot \mathbf{v}_l = 0, \tag{2.1}$$

$$0 = \mu_l \nabla^2 \mathbf{v}_l - \nabla p_l + \rho_l \mathbf{g}, \tag{2.2}$$

where $\mathbf{v}_l$ is the velocity, μ_l is the dynamic viscosity, ρ_l is the density, p_l is the pressure and $\mathbf{g}$ is gravity.

During the derivation we will make use of volume averaging and this requires the distinction between phase averaging and *intrinsic* phase averaging, represented respectively by

$$\langle \psi_l \rangle = \frac{1}{V} \int_{V_l} \psi_l dV, \tag{2.3}$$

$$\langle \psi_l \rangle^l = \frac{1}{V_l} \int_{V_l} \psi_l dV, \tag{2.4}$$

where l is the liquid phase and V is the averaging volume. The reason for the distinction is the inclusion of the solid matrix in the averaging vcolume in addition to the liquid phase, thus we can relate the averages using the porosity of the porous

medium, or equivalently the volume fraction of the liquid phase in the single phase case.

$$\langle \psi_l \rangle = \epsilon \langle \psi_l \rangle^l. \tag{2.5}$$

2.1.1 Continuity equation

Without going into extreme detail we present the spatial averaging of 2.2 as

$$\langle \nabla \cdot \mathbf{v}_l \rangle = \nabla \cdot \langle \mathbf{v}_l \rangle + \frac{1}{V} \int_{A_{ls}} \mathbf{n_{ls}} \cdot \mathbf{v}_l dA = 0. \tag{2.6}$$

This equation can be reduced to the standard continuity equation by application of the no-slip boundary condition on the liquid-solid interface, giving the form

$$\nabla \cdot \langle \mathbf{v_l} \rangle = 0. \tag{2.7}$$

This result is reached by application of spatial averaging although in the derivation of the momentum equation we will make use of the intrinsic spatially averaged continuity equation, of the form

$$\nabla \cdot \langle \mathbf{v}_l \rangle^l = -\frac{1}{\epsilon} \nabla \epsilon \cdot \langle \mathbf{v}_l \rangle^l \tag{2.8}$$

2.1.2 Momentum equation

The phase averaged momentum equation is

$$0 = -\nabla \langle p_l \rangle - \frac{1}{V} \int_{A_{ls}} \mathbf{n}_{ls} p_l dA + \epsilon \rho_l \mathbf{g} + \mu_l \langle \nabla \cdot \nabla \mathbf{v}_l \rangle, \tag{2.9}$$

however it is necessary to make use of the intrinsic phase averaged pressure due to boundary effects. In order to represent this in equation 2.9 we make use of

$$\langle p_l \rangle = \epsilon \langle p_l \rangle^l, \tag{2.10}$$

$$p_l = \langle p_l \rangle^l + \tilde{p}_l, \tag{2.11}$$

where the former equation represents the averaging relation and the latter Gray's decomposition [19]. $\tilde{p}_l$ is the spatial deviation of the pressure from the average. We can then expand the pressure averaged term as

$$\begin{aligned} -\nabla \langle p_l \rangle - \frac{1}{V} \int_{A_{ls}} \mathbf{n}_{ls} p_l dA = & -\epsilon \nabla \langle p_l \rangle^l - \langle p_l \rangle^l \nabla \epsilon \\ & - \frac{1}{V} \int_{A_{ls}} \mathbf{n}_{ls} \langle p_l \rangle^l dA - \frac{1}{V} \int_{A_{ls}} \mathbf{n}_{ls} \tilde{p}_l dA. \end{aligned} \tag{2.12}$$

We now introduce a length scale constraint to the model of the form

$$\left(\frac{r_0}{L_0} \right)^2 << 1, \tag{2.13}$$

where r_0 is the averaging volume characteristic length and L_0 is the macroscopic characteristic length. This requirement is especially important as it states that the final form of Darcy's law must adhere to a definite separation of scale magnitudes in order to be valid. The introduction of this restriction is to allow the transformation

$$\frac{1}{V}\int_{A_{ls}} \mathbf{n}_{ls}\langle p_l\rangle^l dA = \frac{1}{V}\left(\int_{A_{ls}} \mathbf{n}_{ls} dA\right)\langle p_l\rangle^l \tag{2.14}$$

Taking advantage of this relation we can rewrite 2.12 as

$$-\nabla\langle p_l\rangle - \frac{1}{V}\int_{A_{ls}} \mathbf{n}_{ls} p_l dA = -\epsilon\nabla\langle p_l\rangle^l - \frac{1}{V}\int_{A_{ls}} \mathbf{n}_{ls}\tilde{p}_l dA. \tag{2.15}$$

Now that we have the pressure terms we apply the phase averaging twice to the viscous term in equation 2.9 and reduce the resulting terms by applying the no slip condition, resulting in

$$\begin{aligned} 0 = &-\epsilon\nabla\langle p_l\rangle^l - \frac{1}{V}\int_{A_{ls}} \mathbf{n}_{ls}\tilde{p}_l dA + \epsilon\rho_l\mathbf{g} \\ &+ \mu_l\left(\nabla^2\langle \mathbf{v}_l\rangle + \frac{1}{V}\int_{A_{ls}} \mathbf{n}_{ls}\cdot\nabla\mathbf{v}_l dA\right). \end{aligned} \tag{2.16}$$

In a similar manner to the preceding discussion on the pressure term we can apply the following relations to the last term in 2.16

$$\langle \mathbf{v}_l\rangle = \epsilon\langle \mathbf{v}_l\rangle^l, \tag{2.17}$$

$$\mathbf{v}_l = \langle \mathbf{v}_l\rangle^l + \tilde{\mathbf{v}}_l, \tag{2.18}$$

and get the relation

$$\frac{1}{V}\int_{A_{ls}} \mathbf{n}_{ls}\cdot\nabla\mathbf{v}_l dA = -\nabla\epsilon\cdot\nabla\langle \mathbf{v}_l\rangle^l + \frac{1}{V}\int_{A_{ls}} \mathbf{n}_{ls}\cdot\nabla\tilde{\mathbf{v}}_l dA. \tag{2.19}$$

Once again we must apply the intrinsic phase average to the viscous term in 2.16 and apply relation 2.19 to get

$$\begin{aligned} 0 = &-\nabla\langle p_l\rangle^l - \frac{1}{\epsilon V_l}\int_{A_{ls}} \mathbf{n}_{ls}\tilde{p}_l dA + \rho_l\mathbf{g} \\ &+ \mu_l\left(\nabla^2\langle \mathbf{v}_l\rangle^l + \frac{\nabla\epsilon}{\epsilon}\cdot\nabla\langle \mathbf{v}_l\rangle^l + \frac{\langle \mathbf{v}_l\rangle^l\nabla^2\epsilon}{\epsilon}\right) + \frac{\mu_l}{V_l}\int_{A_{ls}} \mathbf{n}_{ls}\cdot\nabla\tilde{\mathbf{v}}_l dA. \end{aligned} \tag{2.20}$$

At this stage we apply an analysis on the orders of magnitude of the terms in 2.20, beginning with scale restriction we imposed earlier, which implies that

$$\tilde{\mathbf{v}}_l = O(l_{cap}), \tag{2.21}$$

where l_{cap} is the capillary radius of the porous medium and we note that $l_{cap} < r_0 < L_0$. From this we can determine the order for the velocity spatial deviation term and relate it to the spatial average.

$$\nabla\tilde{\mathbf{v}}_l = O(\tilde{\mathbf{v}}_l/l_{cap}), \tag{2.22}$$

$$\tilde{\mathbf{v}}_l = O(\langle \mathbf{v}_l\rangle^l/l_{cap}). \tag{2.23}$$

By construction of our equations we know the length scales for $\langle \mathbf{v}_l \rangle^l$, $\langle p_l \rangle^l$ and ϵ are the same, namely the macroscopic scale L_0. Thus we can relate the viscous terms in equation 2.20 to respective orders of magnitude.

$$\frac{\mu_l}{V_l} \int_{A_{ls}} \mathbf{n}_{ls} \cdot \nabla \tilde{\mathbf{v}}_l dA = O(\mu_l \langle \mathbf{v}_l \rangle^l / l_{cap}^2), \tag{2.24}$$

$$\mu_l \nabla^2 \langle \mathbf{v}_l \rangle^l = O(\mu_l \langle \mathbf{v}_l \rangle^l / L_0^2), \tag{2.25}$$

$$\frac{\nabla \epsilon}{\epsilon} \cdot \nabla \langle \mathbf{v}_l \rangle^l = O(\mu_l \langle \mathbf{v}_l \rangle^l / L_0^2), \tag{2.26}$$

$$\frac{\langle \mathbf{v}_l \rangle^l \nabla^2 \epsilon}{\epsilon} = O(\mu_l \langle \mathbf{v}_l \rangle^l / L_0^2). \tag{2.27}$$

From this analysis the viscous terms that do not include the integral are insignificant when compared to the contribution of the the integral term and we can therefore remove them from our formulation, giving us

$$0 = -\nabla \langle p_l \rangle^l - \frac{1}{\epsilon V_l} \int_{A_{ls}} \mathbf{n}_{ls} \tilde{p}_l dA + \rho_l \mathbf{g} + \frac{\mu_l}{V_l} \int_{A_{ls}} \mathbf{n}_{ls} \cdot \nabla \tilde{\mathbf{v}}_l dA. \tag{2.28}$$

In order to close this equation we must determine the spatial deviation terms for pressure and velocity in terms of the spatially averaged values. This process requires the formulation of successive governing equations for the spatial deviation variables until a homogeneous boundary value problem is reached. The logic of this reduction is similar to that used in the steps detailed up to this point and we will not elaborate on them further. We note only that within this reduction the assumption that $\tilde{p}_l$ and $\tilde{\mathbf{v}}_l$ are of equal magnitude is used. Ultimately we get representations of the spatial deviation variables as

$$\tilde{\mathbf{v}}_l = \mathbf{B} \cdot \langle \mathbf{v}_l \rangle^l, \tag{2.29}$$

$$\tilde{p}_l = \mu_l \mathbf{b} \cdot \langle \mathbf{v}_l \rangle^l. \tag{2.30}$$

where $\mathbf{B}$ and $\mathbf{b}$ are arbitrary and appear in the final boundary value problem. Now we can rewrite 2.28 as

$$0 = -\nabla \langle p_l \rangle^l + \rho_l \mathbf{g} + \left(\frac{\mu_l}{V_l} \int_{A_{ls}} \mathbf{n}_{ls} \cdot (\nabla \mathbf{B} - \mathbf{I}\mathbf{b}) dA \right) \cdot \langle \mathbf{v}_l \rangle^l. \tag{2.31}$$

The integral terms have been slightly rewritten to move the averaged velocity term outside of the integral using the justification developed concerning the magnitudes of the length scales, namely $l_{cap} << L_0$. Finally we can rewrite the integral term in the form

$$\mathbf{C} = -\frac{1}{V_l} \int_{A_{ls}} \mathbf{n}_{ls} \cdot (\nabla \mathbf{B} - \mathbf{I}\mathbf{b}) dA, \tag{2.32}$$

and express the phase averaged velocity as

$$\langle \mathbf{v}_l \rangle^l = -\frac{\mathbf{C}^{-1}}{\mu_l} \cdot (\nabla \langle p_l \rangle^l - \rho_l \mathbf{g}). \tag{2.33}$$

We convert to phase average velocity by rewriting the permeability tensor as

$$\mathbf{K} = \epsilon \mathbf{C}^{-1} \tag{2.34}$$

and get the standard form of Darcy's law

$$\langle \mathbf{v}_l \rangle = -\frac{\mathbf{K}}{\mu_l} \cdot (\nabla \langle p_l \rangle^l - \rho_l \mathbf{g}). \tag{2.35}$$

Now that we have successfully derived Darcy's law under the stipulated assumptions we will continue with the understanding that the appropriate spatial averaging has been applied and thus we can write simply

$$\mathbf{v}_l = -\frac{\mathbf{K}}{\mu_l} \cdot (\nabla \langle p_l \rangle^l - \rho_l \mathbf{g}). \tag{2.36}$$

2.1.3 Unsteady formulation

Now that we have derived the steady-state single phase form of Darcy's law we wish to briefly discuss the extension of the equation to include the unsteady term and its implications. We will not explicitly derive the equation but rather discuss the possible forms the unsteady term can take, beginning with the standard unsteady Darcy's law euqations

$$\nabla \cdot (\rho_l \mathbf{v}_l) = 0, \tag{2.37}$$

$$\tau \frac{\partial \mathbf{v}_l}{\partial t} + \mathbf{v}_l = -\frac{\mathbf{K}}{\mu_l} (\nabla \langle p_l \rangle^l - \rho_l \mathbf{g}). \tag{2.38}$$

Note that the only deviation from the previous representation is the addition of the unsteady term in the momentum equation. The difficulty is to properly define the coefficient for the unsteady and there exist several methods for its derivation. Due to the difficulties arising from the implementation of the transient term numerically it is largely ignored on the basis that its effect is limited outside of special cases wherein the permeability is linked to this term at very low Reynolds numbers. Therefore we will only present the possible formulations in the interest of completeness of the theoretical framework as the work undertaken is considered to be transient. The interested reader is encouraged to refer to [20] for a more thorough treatment of unsteady term in Darcy's law. One possible method is to apply the volume averaging technique used in the steady formulation derivation on the Navier-Stokes momentum equation, which gives

$$\tau_{va} = \frac{\mathbf{K} \rho_l}{\mu_l \epsilon}. \tag{2.39}$$

Another representation of τ can be attained by introducing a *virtual mass* coefficient to account for flow accelerations around obstacles, in this case soil particles. The virtual mass coefficient is of the form

$$\tau_{vm} = \frac{\mathbf{K} \rho_l}{\mu_l \epsilon} \left[1 + C_{vm} \frac{1 - \epsilon}{\epsilon} \right], \tag{2.40}$$

where C_{vm} is an empirical coefficient accounting for pore-scale flow inhomogeneities. The final representation of the unsteady term coefficient is based upon volume averaging the kinetic energy equation, resulting in

$$\tau_{en} = \frac{\mathbf{K}\rho_l}{\mu_l} \frac{\langle \mathbf{v}_l \cdot \mathbf{v}_l \rangle}{\langle \mathbf{v}_l \rangle \cdot \langle \mathbf{v}_l \rangle}, \tag{2.41}$$

where the brackets represent spatial averaging as defined previously.

2.2 Porous - free-flow interface

Another aspect to consider when working with Darcy's law is the incompatability of boundary conditions that arises when one wishes to couple a non-porous region to one or several porous regions. This incompatability stems from the theoretical formulations for each region. We have already presented the formulation for flow in porous media but we have not discussed flow in a non-porous region, where inertial effects must be considered. We present the Navier-Stokes equations for single-phase unsteady incompressible flow

$$\nabla \cdot \mathbf{u}_l = 0, \tag{2.42}$$

$$\rho_l \frac{\partial \mathbf{u}_l}{\partial t} + \rho_l(\mathbf{u}_l \cdot \nabla \mathbf{u}_l) = -\nabla p_l + \mu_l \nabla^2 \mathbf{u}_l + \rho_l \mathbf{g}, \tag{2.43}$$

and reiterate the Stokes equation for creeping flow for convenience.

$$\nabla \cdot \mathbf{u}_l = 0, \tag{2.44}$$

$$\rho_l \frac{\partial \mathbf{u}_l}{\partial t} = -\nabla p_l + \mu_l \nabla^2 \mathbf{u}_l + \rho_l \mathbf{g}. \tag{2.45}$$

As we can see in equation 2.43 we have inclusion of the inertial term and thus we cannot combine this with the continuity equation as we can in the case of Darcy's law to remove the dependent variable $\mathbf{u}_l$. Due to this restriction we must provide an additional boundary condition in order to ensure a proper solution. This additional boundary condition for the Navier-Stokes formulation will act on the Darcy's law boundary as an overdetermination of the equation system however we must ensure continuity of both momentum and mass across the interface. This difficulty has been explored relatively thoroughly with the conclusion there is no perfect solution. We present the most common methods to bypass this conundrum by defining the additional boundary condition in terms of the solution of Darcy's law. The most straightforward boundary conditions is the requirement of velocity continuity and its interface-normal gradient.

$$\mathbf{u}_l = \mathbf{v}_l, \tag{2.46}$$

$$\nabla \mathbf{u}_l \cdot \mathbf{n} = \nabla \mathbf{v}_l \cdot -\mathbf{n}. \tag{2.47}$$

This formulation may be straightforward although it doesn't say anything about the velocity behaviour tangential to the interface thus we may experience some

discontiuity or numerical forcing that impacts the accuracy, particularly locally. Another similar formulation applies an effective dynamic viscosity coefficient to the porous media side of the condition, given as

$$\begin{aligned} \mathbf{u}_l &= \mathbf{v}_l, & (2.48)\\ \mu_l \nabla \mathbf{u}_l \cdot \mathbf{n} &= \mu_{l,eff} \nabla \mathbf{v}_l \cdot -\mathbf{n}. & (2.49) \end{aligned}$$

The third formulation introduces the concept of a jump condition that maintains the velocity continuity across the interface however the velocity normal derivative is modified to be

$$\begin{aligned} \mathbf{u}_l &= \mathbf{v}_l, & (2.50)\\ \mu_l \nabla \mathbf{u}_l \cdot \mathbf{n} + \beta_1 \frac{\mu_l}{\mathbf{K}} \cdot \mathbf{u}_l &= \frac{\mu_l}{\epsilon} \nabla \mathbf{v}_l \cdot -\mathbf{n}. & (2.51) \end{aligned}$$

where β_1 is a dimensionless coefficient. This formulation allows for the solution of each domain separately by allowing for different velocity derivatives at the interface. An extension of this jump condition includes an additional term proportional to the velocity squared.

$$\begin{aligned} \mathbf{u}_l &= \mathbf{v}_l, & (2.52)\\ \mu_l \nabla \mathbf{u}_l \cdot \mathbf{n} + \beta_1 \frac{\mu_l}{\mathbf{K}} \cdot \mathbf{u}_l + \beta_2 \rho_l \mathbf{u}_l^2 &= \frac{\mu_l}{\epsilon} \nabla \mathbf{v}_l \cdot -\mathbf{n}. & (2.53) \end{aligned}$$

Once again the additional coefficient β_2 is dimensionless. The final formulation of the boundary interfacial condition is of more interest and was developed by Joseph and Beavers in 1967 [21] and only concerns the free flow velocity derivative at the interface.

$$\begin{aligned} \mathbf{u}_l &= \mathbf{v}_l, & (2.54)\\ \nabla \mathbf{u}_l \cdot \mathbf{n} &= \frac{\alpha^*}{\mathbf{K}} \cdot (\mathbf{u}_{l,int} - \mathbf{u}_{l,\infty}), & (2.55) \end{aligned}$$

where α^* is a dimensionless slip coefficient, $\mathbf{u}_{l,int}$ is an interfacial velocity and $\mathbf{u}_{l,\infty}$ is the free-flow velocity. It is worthwhile to note at this point that while this condition has been proven rigorously consistent by [22] for single phase flows there is no such backing for its extension to multiphase flows even though it is commonly used in such cases.

2.3 Extending single phase equations to multiphase

In general, the extension of single phase equations to multiphase is straightforward; define a set of equations for each fluid phase and a scalar variable equation representing the fraction of each phase present in a single averaging (or computational) volume. Darcy's law can be extended to multiphasic systems by including a subscript $\omega(= \eta)$,

giving

$$\omega = l, a, \tag{2.56}$$

$$\omega_l + \omega_a + \epsilon = 1, \tag{2.57}$$

$$\frac{\partial \alpha_\omega}{\partial t} + \nabla \cdot \mathbf{v}_\omega = 0, \tag{2.58}$$

$$\mathbf{v}_\omega = -\frac{\mathbf{K}_\omega}{\mu_\omega} \cdot (\nabla \langle p_\omega \rangle^\omega - \rho_\omega \mathbf{g}) + \mathbf{K}_{\omega\eta} \cdot \mathbf{v}_\omega, \tag{2.59}$$

where α_ω is the volume fraction of each phase and $\mathbf{K}_{\omega\eta}$ represent viscous drag effects of one phase upon the other. It is worthwhile to mention that $\mathbf{K}_{ls} \neq \mathbf{K}_{sl}$ and that these terms can be considered negligible when the magnitude difference of the viscosities is non-unity. The discussion surrounding these terms and the details of the derivation for multiphase Darcy's law can be found in Whitaker [23] though it is beyond the scope of this work.

In single phase Darcy's law we only considered a single permeability K however in multiphase we now have to consider the interactions between the solid matrix and the fluid phases in addition to their effects on each other. This requirement leads to the introduction of *relative permeability* $k_{r\omega}$ and its mathematical relationship to (absolute) permeability

$$\mathbf{K}_\omega = k_{r\omega}\mathbf{K}. \tag{2.60}$$

We must be very careful when representing the permeabilities in this manner as the interactions described are not isotropic and the exact relation between these quantities is unknown therefore we are forced settle for a coefficient. Additionally we note that the relative permeability is not isotropic either and should be a tensor. The difficulty in determining such a complex tensor experimentally or numerically means we simplify it to a scalar between 0 and 1 though the sum of relative permeabilities needn't be unity.

2.4 Relative permeability and variable saturation

When working with a single phase subsurface flow problem we can experimentally determine the permeability of the solid matrix however with the addition of more phases and consequently relative permeability, we must construct a relationship between the two phases. This interaction aims to capture lubricating effects on the solid matrix, capillary suction and interpenetration of the phases. When we say interpenetration of the phases we must stress that the phases are considered immiscible and the only possible mass transfer must occur via condensation/evaporation. As we have not introduced temperature dependence this will not be considered further. The phase interaction represented by relative permeabilities is by its construction phasic volume fraction dependent thus we must introduce the concepts of saturation and volumetric water content. Volumetric water content is denoted by θ and can be related to saturation by

$$S_l = \frac{\theta}{\epsilon}, \tag{2.61}$$

for a representative volume. It is important to stress that saturation is not equivalent to effective saturation (also known as normalized water content) which is defined as

$$S_e = \frac{\theta - \theta_r}{\theta_s - \theta_r}, \tag{2.62}$$

where θ_s is saturated volumetric water content and θ_r is residual volumetric water content. There are several models to relate effective saturation to capillary pressure or pressure head such as the Brooks-Corey model [24] used in the oil and gas industry however the most common model in use is the van Genuchtem-Mualem model (VGM).

$$S_e = [1 + (p_c/p_g)^n]^{-m}, \tag{2.63}$$
$$m = 1 - 1/n, \tag{2.64}$$

where p_c is the capillary pressure, p_g is a pressure scaling value, and m and n are fitting coefficients related to the pore size distribution. Capillary pressure is defined as

$$p_c = (p_a - p_l). \tag{2.65}$$

In order to complete the relationship between relative permeability and effective saturation we must introduce hydraulic conductivity, which describes the ability of liquid to flow through the pore spaces of a porous medium. It is related to permeability by

$$\mathbf{K} = \kappa \frac{\mu_l}{\rho_l \mathbf{g}}. \tag{2.66}$$

Now that we can relate permeability and hydraulic conductivity we can define the relationship we require accordingly as

$$\kappa(S_e) = \kappa_s \kappa_r(S_e), \tag{2.67}$$
$$\kappa(S_e) = \kappa_s S_e^q (1 - (1 - S_e^{1/m})^m)^2, \tag{2.68}$$

where κ_s is the saturated hydraulic conductivity and q is a model parameter representing the pore connectivity. Our equation system is now closed. If we wish to use the VGM model, we only require the coefficient values and easily measurable material properties although generally this requires extensive and difficult experimentation to correctly determine their values. As an alternative we will calculate this relationship directly at the mesoscale. Before we do this we will touch on an additional issue arising when attempting to include variable saturation in traditional CFD simulations.

2.5 Variable saturation and mass conservation

When working with multiphase systems we must track the interface between the phases in order to accurately determine the volumetric volume fractions for each phase. This can be done using a variety of techniques including Volume of Fluid (VOF), Level-set Method (LSM) and immersed boundary method (IBM). In most cases the phase volume fractions are computed at every iteration of the simulation for

all cells. We will focus on the VOF method in Fluent 17.1 and discuss the problems that arise when implementing variable saturation. In Fluent 17.1 the VOF model interphase tracking (mass conservation) is

$$\frac{1}{\rho_\omega}\left[\frac{\partial}{\partial t}\left(\alpha_\omega \rho_\omega\right) + \nabla \cdot \left(\alpha_\omega \rho_\omega \mathbf{v}_\omega\right) = S_{\alpha\omega} + \sum_{\eta=l,a}\left(\dot{m}_{\eta\omega} - \dot{m}_{\omega\eta}\right)\right], \tag{2.69}$$

where $S_{\alpha\omega}$ is a phasic source term and $\dot{m}_{\eta\omega}$ is mass transfer from phase η to ω. The issue becomes plain if we examine the equation for multiphase scalar transport.

$$\frac{\partial}{\partial t}\left(\alpha_\omega \rho_\omega \phi_\omega\right) + \nabla \cdot \left(\alpha_\omega \rho_\omega \mathbf{v}_\omega \phi_\omega\right) = \nabla \cdot \left(\alpha_\omega \Gamma_\omega \nabla \phi_\omega\right) + S_{\phi,\omega}, \tag{2.70}$$

where ϕ_ω is any scalar quantity and Γ_ω is the diffusion coefficient. If we recall previously that since both effective saturation and volumetric fractions range from 0 to 1 and represent the quantity of liquid vs. air in a volume, they are essentially identical. We can safely argue that diffusion is a non-negligible process with regard to saturation and therefore the diffusion term must be present in any transport equation. This disconnect between the two equations will cause a myriad of inaccuracies, particularly in mass conservation, in the solution of the entire system, rendering the result useless. In order to rectify this problem a correction factor must be used and tuning this unphysical correction term is time consuming and must rely on experimentation to adjust accurately for each unique case. Another method to account for this disconnect is to solve for saturation on a smaller scale using the Lattice Boltzmann method.

Chapter 3

Mesoscale simulations using Lattice Boltzmann

3.1 The Lattice Boltzmann Method

We begin with a short background of the Lattice Boltzmann method (LBM) and a derivation of the discrete Boltzmann equation. This is followed by its application to our problem regarding saturation and relative permeability over time.

3.1.1 The Boltzmann equation

The Lattice Boltzmann method is an alternative to the traditional Navier-Stokes approach by solving the Boltzmann equation. It can be applied to the mesoscopic scale as well as the macroscopic scale, depending on the desired resolution and problem scale. While it has advantages over traditional CFD modeling I do not believe it can be used as a substitute due to the extensive background enjoyed by CFD. The original method to use this approach was developed in the 1950s by Ulam and von Neumann and was called the Lattice Gas Automaton. The method has been modified since its earliest form and is experiencing a resurgence in interest due to its capacity for handling multiphase flows in complex geometries, among other benefits. Once again we will present a brief derivation of the discrete Boltzmann equation that is solved in LBM and stress the assumptions required for its application. A more complete derivation can be found in [25]. Similarly to the derivation of Darcy's law the background provided by this derivation is useful both for understanding exactly how the method works but also its inherent limitations.

Before we can present the Boltzmann equation we must discuss the idea of a phase space and a corresponding density function. A phase space is defined as a space in which every state of a system corresponds to a single point within the space. In our case it is defined by positional coordinates $\vec{x}$ and momenta $\vec{p} = M\vec{v}$ where M is mass and $\vec{v}$ is velocity. The space is 6-dimensional and each position is parametrized by time t. Thus a differential elementary volume can be written as

$$d^3\vec{x}d^3\vec{p} = dxdydzdp_xdp_ydp_z, \tag{3.1}$$

and the corresponding density function $f(\vec{x}, \vec{p}, t)$ is defined such that the probable number of particles in the volume is given by

$$N = \int d^3\vec{p} \int d^3\vec{x} f(\vec{x}, \vec{p}, t). \tag{3.2}$$

We can now represent the general Boltzmann equation in terms of the density distribution function by

$$\frac{df}{dt} = \left(\frac{\partial f}{\partial t}\right)_{force} + \left(\frac{\partial f}{\partial t}\right)_{diff} + \left(\frac{\partial f}{\partial t}\right)_{coll}, \tag{3.3}$$

where the force term represents any external force applied to the particles, the diffusion term represents particle diffusion, and the collision term represents inter-particle collisions. After some re-representation of the force and diffusion terms we can rewrite equation 3.3 by balancing these terms against the collision term.

$$\frac{\partial f}{\partial t} + \frac{\vec{p}}{M} \cdot \nabla f + \vec{F} \cdot \frac{\partial f}{\partial \vec{p}} = \left(\frac{\partial f}{\partial t}\right)_{coll}. \tag{3.4}$$

Before we can solve this equation we must find a representation for the collision term. Deriving this term requires knowledge of statistical mechanics beyond the scope of this work however we will give its representation and most common simplified form in the interest of completeness.

$$\left(\frac{\partial f}{\partial t}\right)_{coll} = \int (\hat{f}_{12} - f_{12}) \vec{g} I(\vec{g}, \Omega) d\Omega d\vec{p}_{12}, \tag{3.5}$$

where $\hat{f}_{12}$ is the post-collision distribution of particles 1 and 2, $\vec{g} = \vec{v}_1 - \vec{v}_2$ is the relative velocity between the particles, I is the differential cross-section of the collision and Ω is the characteristic angle of collision. It is important to note that in order to calculate such interactions Boltzmann applied the argument of so-called *Stosszahlansatz*, or "molecular chaos". This argument states that while the probabilities or two particles colliding is reliant on the collisions of other particles with them *ad infinitum*, however we can consider their distribution functions independent of each other, such that

$$f_{12} = f_1 f_2, \tag{3.6}$$

and consequently we can rewrite equation 3.5 as

$$\left(\frac{\partial f}{\partial t}\right)_{coll} = \int \int (\hat{f}_1 \hat{f}_2 - f_1 f_2) \vec{g} I(\vec{g}, \Omega) d\Omega d\vec{p}_1 d\vec{p}_2. \tag{3.7}$$

For covenience when describing the the discrete Boltzmann equation we can rewrite 3.4 in terms of a streaming operator $\mathscr{S}$ and a collision operator $\mathscr{C}$.

$$\mathscr{S} f = \mathscr{C}_{12}. \tag{3.8}$$

In addition we can relate the macroscopic quantities density ρ, momentum $\rho\mathbf{v}$ and energy density ρe to the collision invariants. These collision invariants are the particle number, momentum and energy. These quantities are related by

$$\rho = M \int f d\vec{v}, \tag{3.9}$$

$$\rho\mathbf{v} = M \int f d\vec{v}, \tag{3.10}$$

$$\rho e = M \int f \frac{\vec{v}^2}{2} d\vec{v}. \tag{3.11}$$

The few final notes on the Boltzmann equation deal with equilibria. The distribution function satisfies the condition of local equilibirium, that is particles entering the element are balanced with those exiting. In addition, fluids tend to local equilibrium and this process is called local equilibrium relaxation. This relaxation takes place from one-body distribution to local equilibrium among particles and finally to global equilibrium over the domain. It is therefore unsurprising that one can link the particle kinetics to macroscopic scale theory by spanning ever-larger time scales. It is possible to derive the Navier-Stokes equations of motion from the Boltzmann equation by expanding the variables appropriately. This is done by applying the Chapman-Enskog expansion however the details are beyond the scope of this work.

3.1.2 Lattice-Gas Cellular Automata

In order to reach the discrete Boltzmann equation formulation we must start with the theory behind the predecessor of LBM, the Lattice-Gas Cellular Automata (LGCA). In this method a cell is composed of nodes and vectors connecting them to each other. The cell can be a variety of shapes in 2 and 3 dimensions but we shall focus on a square 2-dimensional lattice for our explanation. The vectors connecting the nodes are given as $\vec{c}_r = [c_{ri}, c_{rj}]$ where r is a node number a i, j are Cartesian coordinates x, y. There are a few rules for lattice occupancy, namely:

- All particles have the same mass, $M = 1$.
- A particle can move only in one direction in a single time interval.
- A particle moves from $\vec{x}$ to $\vec{x} + \vec{c}_r$.
- Two particles in the same position cannot move in the same direction.

These rules allow for a cell to hold up to 8 fluid particles simultaneously at a single time instant and we therefore define an occupancy number n_r to define the possible states

$$n_r(\vec{x}, t) = 0, \text{ no particles present}, \tag{3.12}$$

$$n_r(\vec{x}, t) = 1, \text{ a particle is present}. \tag{3.13}$$

The streaming and collision operators given in the compressed Boltzmann equation 3.8 can be written in discrete format to describe a particle's motion in the lattice by

$$\begin{aligned} \mathscr{S}_r n_r &= n_r(\vec{x}+\vec{c}_r, t+1) - n_r(\vec{x}, t), && (3.14)\\ \mathscr{C}_r(n_1, ..., n_9) &= \tilde{n}_r(\vec{x}, t) - n_r(\vec{x}, t), && (3.15)\\ \mathscr{S}_r n_r &= \mathscr{C}_r(n_1, ..., n_9), && (3.16) \end{aligned}$$

where $\tilde{n}_r$ is the post-collision state. In order to recover the Navier-Stokes equations the collisions in this system must satisfy conservation of mass and momentum. In addition, the cells must be shaped such that the rotational invariance of the Navier-Stokes stress and strain tensor elements is properly captured.

3.1.3 The Lattice Boltzmann equation

An improvement upon the LGCA was developed by McNamara and Zanetti [26] in 1988 that removes the occupancy number Boolean values and replaced them with a mean and fluctuating value

$$n_r = f_r + r_r, \tag{3.17}$$

where f_r is the spatial and temportal mean value of the occupancy number. This modification meant that rather than fixing particles to a specific point, each location is assigned a mean probability of finding a particle at that location. The motivation for this change was to reduce statistical noise which was present in the LGCA. Substituting equation 3.17 into 3.16 we get

$$\mathscr{S} f_r = \mathscr{C}_r(f_1, ..., f_9) + R_r, \tag{3.18}$$

where R_r is the sum of the fluctuations. Due to the concept of molecular chaos mentioned earlier all particles are uncorrelated and thus all have the same probabilities thus $R_r = 0$. Thus the non-linear Lattice Boltzmann is written as

$$\mathscr{S} f_r = \mathscr{C}_r(f_1, ..., f_9). \tag{3.19}$$

In order to overcome the nonlinearity of the collision operator the Chapman-Enskog expansion was suggested by both McNamara and Zanetti [26] as well as Higuera and Jimenez [27] to generate the quasi-linear Lattice Boltzmann equation

$$\mathscr{S} f_r = \mathscr{A}_{r_1 r_2}(f_{r_1} - f^e_{r_2}), \tag{3.20}$$

where r_1, r_2 are distinct directions and $\mathscr{A}$ is a scattering matrix. A further modification of this equation resulted in the Lattice-Bhatnagar-Gross-Krook (LBGK) model. This model replaced the scattering matrix with a single parameter τ_f to define the physics of the fluid and is written as

$$\mathscr{S} f_r = -\frac{1}{\tau_f}(f_{r_1} - f^e_r). \tag{3.21}$$

This model is also known as the single time relaxation model and requires the satisfaction of the conditions:

$$\rho = \sum_r f_r^e = \sum_r f_r, \tag{3.22}$$

$$\rho v_i = \sum_r f_r^e c_{ri} = \sum_r f_r c_{ri}. \tag{3.23}$$

The equilibrium distributions f_r^e must be chosen to correctly reflect the Navier-Stokes equations in terms of conservation and depend on the choice of cell dimension and shape. In addition there is some restriction of the choice of τ_f as it is related to fluid kinematic viscosity by

$$\nu = c_s^2(\tau_f - 0.5), \tag{3.24}$$

where c_s is a speed of sound coefficient. From this we can see that values of τ_f below 0.5 will induce a negative viscosity and if we increase it too much we will increase the fluid viscosity similarly.

3.1.4 The Washburn equation

The last theoretical concept we will introduce related to LBM is the usage of the Washburn equation to calculate an analytical solution for saturation over time in a tube as a guide for our simulation results. The Washburn equation is given as

$$h_c^2(t) = \frac{\gamma \cos(\theta_c) R_c}{2\mu_l} t, \tag{3.25}$$

where h_c is the liquid penetration depth along the main flow direction, γ is the surface tension, θ_c is the liquid-air contact angle and R_c is the capillary radius. it describes the capillary rise of liquid in a pore or tube without external forces. It can be derived from the Stokes equation for flow in a pipe of constant radius and applying an initial condition of $h(0) = 0$. We neglect the intertial term as our flow is of sufficiently low velocity that it will be negligible and the resulting equation is

$$h_c(t) = \left(\frac{\gamma \cos(\theta_c) R_c}{2\mu_l} - \frac{\Delta P}{L_p} \frac{l_{\Delta P} R_c^2}{4\mu_l} \right)^{\frac{1}{2}} t^{\frac{1}{2}}, \tag{3.26}$$

where $l_{\Delta P}$ is the liquid volume thickness. By taking an analogue for the definition of saturation we can nondimensionalize equation 3.26 an relate it to saturation. This analogue is based upon arguing that the liquid volume present as a function of time can be related to capillary rise if we look at the domain as a singular volume, thus we can argue

$$S_l(t) = \frac{V_l}{\epsilon V} \approx \frac{\langle h_c(t) \rangle}{L_p}, \tag{3.27}$$

and subsequently

$$S_l(t) = \left(\frac{\gamma \cos(\theta_c) R_c}{2\mu_l L^2} - \frac{\Delta P}{L_p} \frac{l_{\Delta P} R_c^2}{4\mu_l L^2} \right)^{\frac{1}{2}} t^{\frac{1}{2}}. \tag{3.28}$$

By grouping the terms as ratios between capillary and viscous forces, and pressure gradient and viscous forces, respectively, we can rewrite equation 3.28 in terms of a dimensionless time t^*

$$U_\gamma = \frac{2\gamma\cos(\theta_c)R_c}{\mu_l L}, \tag{3.29}$$

$$U_{\Delta P} = -\frac{\Delta P}{L_p}\frac{l_{\Delta P}R_c^2}{4\mu_l L}, \tag{3.30}$$

$$t^* = \frac{(U_{\Delta P}+U_\gamma)}{L}, \tag{3.31}$$

$$S_l(t) \approx \frac{1}{2}t^{*\frac{1}{2}}. \tag{3.32}$$

This result will be used in chapter 4 to give an idea of the accuracy of the simulations when compared to an ideal capillary system. Note that this analytical result is based upon a constant capillary radius, which does not reflect our cases but it is useful as a guide on the temporal dynamics of the system. We are now ready to implement the therotical framework discussed in this chapter in a LBM code.

3.2 Implementation of LBM

During the course of the work with Lattice Boltzmann the open source code developed by Dario Maggiolo was used [28]. It is capable of handling multiphase flow with the caveat that the density difference must not exceed 10^4, which holds for our case of air and water. Moreover the code allows for thermal effects should this be desired; in the current work this is neglected.

Lattice generation

Before any simulations can be run a binary 3D lattice must be generated, representative of the desired soil geometry. There are a myriad of approaches that may be taken to accomplish this task, from structured or randomized volume packing algorithms to image analysis of X-ray tomography scans. The approach used here takes advantage of an modeling software called Blender, which can handle a large number of objects and apply simple collision physics to allow for a randomized packing in a chosen volume. The volume dimensions are chosen such that they adhere to restrictions regarding wall effects on the calculated flow field [29]. It is common practice to ensure the boundaries are at least 15-20 times the particle diameter perpendicular to the flow direction to ensure the minimization of wall effects, thus we must determine the appropriate particle diameter.

The spherical particle diameter is calculated from the desired pore-size that you wish to resolve using LBM. In this case there is information available on the typical pore sizes of lightweight expanded clay aggregates (LECA) [30]. It is alternatively possible to simply determine by experimentation your particle size-distribution and either generate a representative quantity of particles or choose a mean approximation.

In order to determine the equivalent grain size from our resolved pore size we apply the Revil, Glover, Pezard and Zamora (RGPZ) model [31], [32] which states

$$d_{eff} = 2\Theta r_{eff}, \tag{3.33}$$

$$\Theta = \sqrt{\frac{ew^2}{8\epsilon^{2w}}}, \tag{3.34}$$

where e is a parameter valued 8/3, w is the cementation exponent valued 1.5 for spherical particles and ϵ is the porosity.

In the software Blender the spheres are initialized in the desired quantity, in this case 5376, above the domain box and are allowed to fall and interact with each other by application of rigid body physics (collision with no deformation). These spheres can be considered randomly packed and this method of packing has been validated for use as such in [33]. We give an example of such a packing being formed by the falling spheres in Blender in Figure 3.1. The spheres within the box will be converted into the lattice using MATLAB.

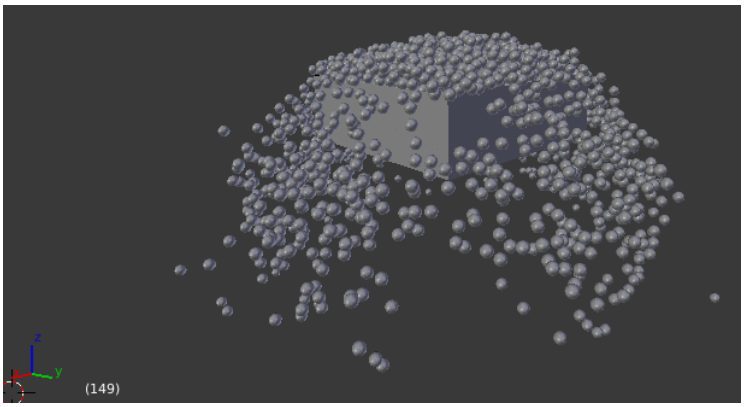

Figure 3.1: Blender simulation of randomly packed spheres after 150 seconds.

The spheres' center coordinates are tracked over a sufficient number of frames until they come to rest and the final values are exported for use in the lattice generation. In order to generate the binary lattice we determine an appropriate number of nodes for each direction that allow us to capture the geometry accurately and is determined by testing. Due to the nature of the restriction on domain size we mentioned previously and the resolution requirements we find the simulation complexity can increase extremely quickly, as demonstrated by Table 3.1.

To generate the lattice a MATLAB code is used to detemine which nodes are solid and which are void spaces based upon sphere radii and node location. Note that in Blender the spheres are detemined by physical measurements however the lattice has no metric, thus the conversion must be done to preserve the integrity of the packed spheres. An example of the conversion can be found in Figure 3.2. This conversion preserves only the sphere centers and approximates as best as possible the full sphere volumes however before we can use the lattice we must add a non-porous zone above the porous zone to contain the liquid and we add walls as well. Once this is done the lattice is ready to use in the LBM code.

Table 3.1: Lattice node quantities for several grid resolutions.

	NZ	NX	NY	Total Nodes
Grid 1	50	150	150	1.125×10^6
Grid 2	60	180	180	1.994×10^6
Grid 3	70	210	210	3.087×10^6
Grid 4	80	240	240	4.608×10^6
Grid 5	140	420	420	2.4696×10^7

(a) Converted lattice, $NZ = 70$. (b) Free-flow and walls added, $NZ = 140$.

Figure 3.2: Conversion and modification of Blender domain, 2D slice at $X = 105$.

In the rest of this document we will discuss different cases run on a single lattice. This lattice is defined in Table 3.1 as Grid 3. This lattice consists of a domain measuring $Z \times X \times Y = 1.0 \times 1.5 \times 1.5$ [cm]. of which half is porous media. This domain is pictured in Figure 3.3

Non-dimensionalized simulation inputs

In this code all inputs into the LBM simulation must be non-dimensional and here we discuss the method by which the conversions are done with regard to the code in use. We begin with 3 characteristic lengths that will be used

$$L = 1.5 \times 10^{-2}[m], \tag{3.35}$$
$$h = 2.5 \times 10^{-3}[m], \tag{3.36}$$
$$d = 7.4 \times 10^{-4}[m], \tag{3.37}$$

which are defined as the domain length perpendicular to the direction of flow, the standing water height and the soil particle diameter, respectively. From these values and a choice of lattice resolution we can convert from metric units to LBM units with relative ease.

$$L_{LB} = 210, \tag{3.38}$$
$$\Delta x_{vox} = \frac{L\Delta x_{LB}}{L_{LB}} = 7.14 \times 10^{-5}[m], \tag{3.39}$$
$$d_{LB} = \frac{d\Delta x_{LB}}{\Delta x_{vox}} = 10.4. \tag{3.40}$$

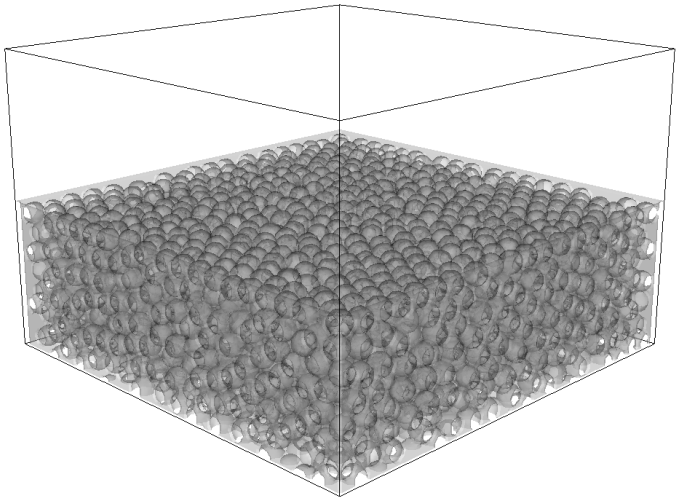

Figure 3.3: 3D lattice reconstruction, $[140, 210, 210] = [1.0, 1.5, 1.5]$ [cm].

Note here that the lattice increment is 1. Any desired conversion can be done in this way and we will only provide some relevant relations that are used in the course of the work.

$$U = \frac{K}{\mu_l}\left(\frac{\Delta P}{L}\right) = \frac{Re\nu_l}{d}, \tag{3.41}$$

$$Bo = \frac{\Delta\rho g h^2}{\gamma}, \tag{3.42}$$

$$g = \frac{\gamma}{\Delta\rho h^2 Bo}, \tag{3.43}$$

$$t = t_{LB}\frac{L^2}{L_{LB}^2}\frac{\nu_{l,LB}}{\nu_l}, \tag{3.44}$$

$$\overline{K} = \frac{\overline{U}\mu_l}{\left(\frac{\Delta P}{L}\right)L^2}, \tag{3.45}$$

$$Re = \frac{Kd}{\mu_l\nu_l}\left(\frac{\Delta P}{L}\right). \tag{3.46}$$

where U and $\overline{U}$ are the velocity and spatially averaged velocity, K is the permeability, ν_l is the kinematic viscosity, g is the gravitational constant, γ is surface tension, Bo is the bond number and represents the ratio of gravitational forces to surface tension and Re is the Reynolds number representing the ratio of viscous and interial forces. In Table 3.2 we present the dimensional anad non-dimensional values for the parameters of interest. In our simulations we have chosen the standard liquid height h to be 2.5 [mm], resulting in a bond number of approximately 1. From this we can back calculate the pressure difference in lattice units since these equations are valid for both physical values and lattice unit equivalencies. We now have the necessary to run the simulations, beginning with single phase.

Table 3.2: Physical and non-dimensional constants.

Quantity	Non-dim. value	Physical value	Unit
L	210	15	[mm]
h	15/35/50	1/2.5/3.6	[mm]
d	10.4	0.74	[mm]
μ_l	2.4/6	1.00e-3	[Ns/m^2]
μ_a	0.12/6	1.68e-7	[Ns/m^2]
ν_l	1/6	1.00e-6	[m^2/s]
ν_a	1/6	1.27e-5	[m^2/s]
ρ_l	2.4	998	[kg/m^3]
ρ_a	0.12	1.20	[kg/m^3]
γ	0.093	0.074	[N/m]

3.2.1 Single phase simulations

Before running simulations to determine saturation we undertake a grid resolution test. We do this to determine the optimal resolution to capture the flow without unnecessary computation time and effort. This is accomplished by increasing and decreasing the number of nodes and generating a new lattice accordingly. Simulations are run for 10,000 iterations and the determination of grid resolution accuracy is accomplished by calculating the permeability as well as checking the Reynolds number.

Table 3.3: Grid resolution test case input and results.

Case	dPdL	Re	Permeability	% Error
Grid 1	6.53E-5	0.00195	1.39E-6	-
Grid 2	4.53E-5	0.00221	1.29E-6	7
Grid 3	3.30E-5	0.00245	1.22E-6	5
Grid 4	2.55E-5	0.00276	1.18E-6	3

The selection of the appropriate grid is reliant on the acceptable error tolerance upon grid refinement. In our case we are comfortable with the 5% relative error thus we choose the Grid 3 and its solution for single phase air flow as the starting point for the multiphase simulations.

3.2.2 Multiphase simulations

Once the appropriate grid resolution has been chosen, in our case Grid 3 where $L = 210$, we can extend the simulations to include rainfall imbibition and drainage. The lattice must be modified accordingly to incorporate surface water or water already present in the soil matrix. In our case we simply define a height of water directly above the porous medium across the domain.

The additional parameters required to run the simulations in multiphase is the density of the liquid phase and the contact angle of the walls (also interpreted as hydrophilicity/phobicity of the solid matrix. This quantity is represented in the code as ρ_{wall}. It is important to mention that we do not modify the gravity (or pressure difference) value from the single phase base case as this would disrupt the simulation. The liquid density is

$$\rho_{l,LB} = 2.4, \tag{3.47}$$

and the values for ρ_{wall} range from 0.03 to 0.06. The details concerning contact angles and their effect on the flow will be discussed in Chapter 4. After the liquid phase has been defined in the lattice and the new parameters chosen the simulations are run wherein the liquid simply infiltrates the porous medium driven only by gravity. The simulation is run sufficiently long as to allow full imibibition or drainage to take place or for a desired number of iterations. After it is complete the results are exported for a desired number of timesteps and the results can be analyzed.

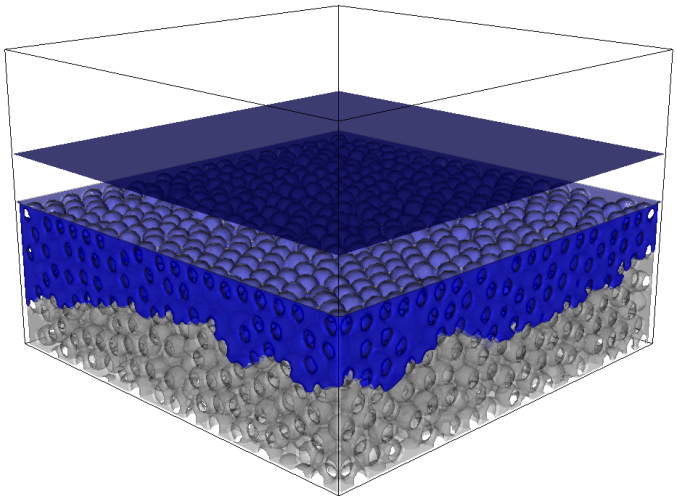

Figure 3.4: Infiltration on Grid 3, example at iteration 150,000.

An example of how these simulations look after a given number of timesteps is shown in Figure 3.4. The exported quantities, excluding thermal and chemical reactions, are the velocity vector, density, and the lattice information. With this information it is possible to calculate several quantities of interest, most notably permeability, porosity, average velocity, pore size distribution and saturation. It is worthwhile to note that to ensure no effects from the walls are included we only perform analysis on the interior two-thirds of the domain perpendicular to the flow. The analysis of a variety of multiphase cases is presented in the next section.

Chapter 4

Results

4.1 The effect of contact angles on saturation

The first tests carried out using LBM investigated the effect of variable contact angles on the flow and consequently the saturation over time. This investigation was undertaken over a variety of cases with the aim of quantifying and understanding the magnitude of effect this variable has on the results. As it is an easy modification within the code and can be controlled in the design process it is a relative parameter to study. The cases studied are outlined in detail below and will be henceforth referred to in the manner presented within the table.

Table 4.1: Multiphase cases run using LBM, OC - old code, NC - new code, ZV - no single phase convergence prior to multiphase.

Case	h	ρ_{wall}	Additional Notes
MP 1	35	0.06	OC
MP 2	35	0.03	OC+NC
MP 3	35	0.04	OC
MP 4	50	0.04	OC
MP 5	50	0.06	OC
MP 6	50	0.03	OC+NC
MP 7	35	0.06	NC, ZV
MP 8	15	0.04	NC

The 8 cases are categorized by water film height (or hydraulic pressure applied) h and contact angle (or hydrophilicity) ρ_{wall} where the angles correspondly relate as

$$0.06 = 72^{\circ}, \tag{4.1}$$
$$0.04 = 78^{\circ}, \tag{4.2}$$
$$0.03 = 81^{\circ}. \tag{4.3}$$

These values are taken from the old code but since the majority of the cases were run in this way we will use these as the standard. It is sufficient to note that the

differences between the values from each code are minimal but it is mentioned in the interest of clarity.

We have plotted saturation over time for the simulations and compared the results to the theoretical solution for saturation as a function of time as given in equation 3.32. As we can see the result matches fairly well for the case of higher hydrophilicity (Figure 4.1a) however in the case nearest to neutrality, 4.1c, we see a complete failure of liquid imbibition. This result will be tackled in more detail later in this section. As for the case of no single phase convergence prior to adding water, as seen in 4.1b, we see a delay in the imbibition at the beginning but the slope quickly establishes itself in accordance with the first case as expected. Similarly we can see quite clearly that in Figure 4.1d that the imbibition is delayed but after some time the slope matches that of the higher hydrophilicity cases.

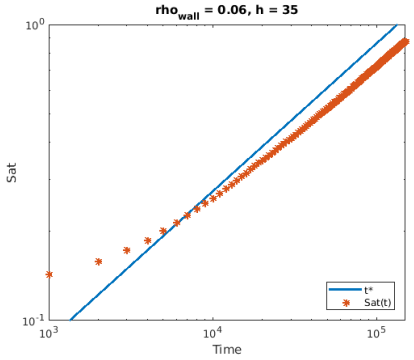

(a) Case MP 1.

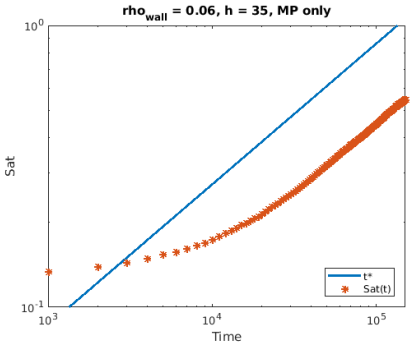

(b) Case MP 7, no single phase prior.

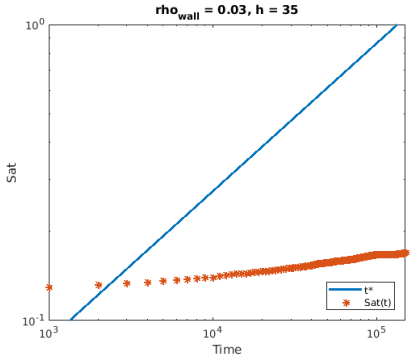

(c) Case MP 2.

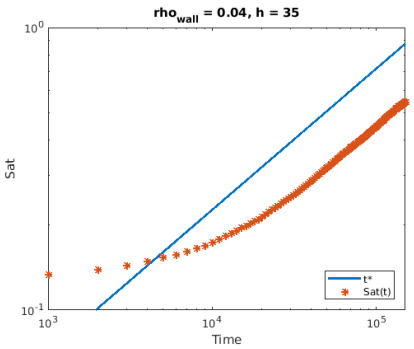

(d) Case MP 3.

Figure 4.1: Effect of contact angle on saturation over time.

Since case MP 2 seems to be problematic we need to be sure that there is no error with the lattice resolution. This is checked by increasing the pressure head, modifying the water height from $h = 35$ to $h = 50$ and reducing case MP 3 to $h = 15$ to see if we can recreate the bloacking effect. Once again the results are plotted and we can immediately see a few interesting changes. In Figure 4.2a we see a slightly better convergence to the theoretical result and in 4.2d we see a slight increase in hydraulic head results in very little difference in saturation. The most interesting cases are 4.2b and 4.2c, where we approach the blockage scenario encountered in 4.1c. The implication here is that we can force imbibition by increasing hydrophilicity

simultaneously with pressure head reduction OR simply increase the hydraulic head and keep hydrophilicity steady.

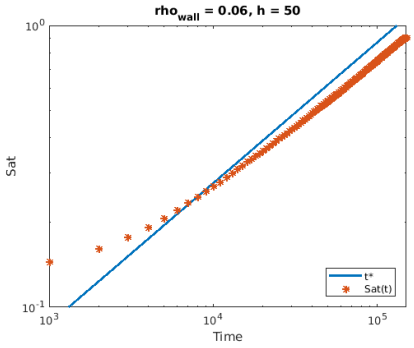

(a) Case MP 5.

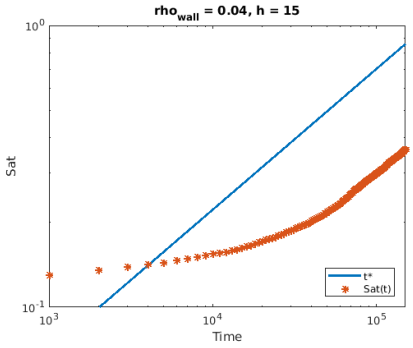

(b) Case MP 8.

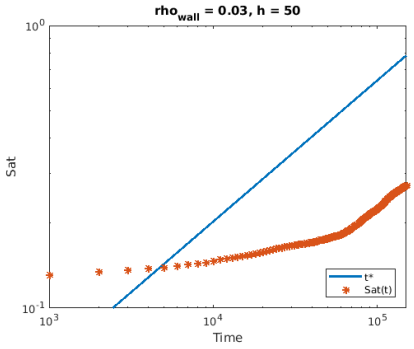

(c) Case MP 6.

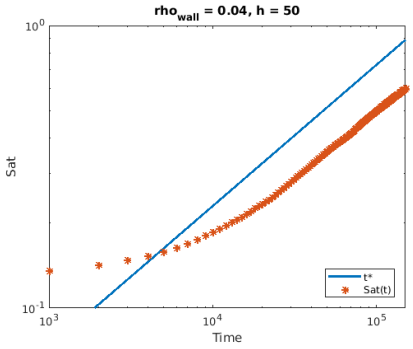

(d) Case MP 4.

Figure 4.2: Effect of contact angle on saturation over time.

These results are in keeping with physical theory and thus we can be confident the simulations are capturing the phenomena accurately however there may still be the issue with lattice resolution. We test this by running case MP 2 on a higher resolution lattice and check if the imibibition is improved.

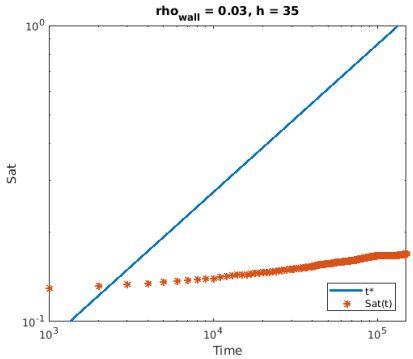

(a) Case MP 2.

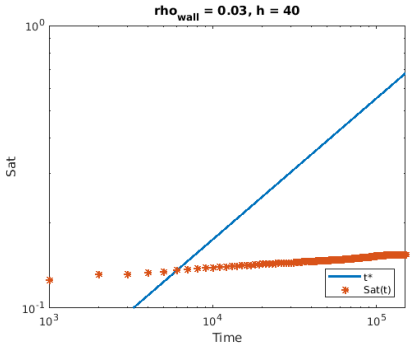

(b) Case MP 2 with lattice [160 240 240].

Figure 4.3: Effect of increasing lattice resolution on case MP 2.

As we can see, the lattice resolution increase has no effect on the imbibition over time and thus we can safely conclude the effect we are witnessing is accurate

and stems from the capillary nature of the domain itself in combination with the contact angle. To check if this case and its higher hydraulic head analogue eventually converge we extend the length of the simulation from 150,000 iterations to 450,000 and plot the results.

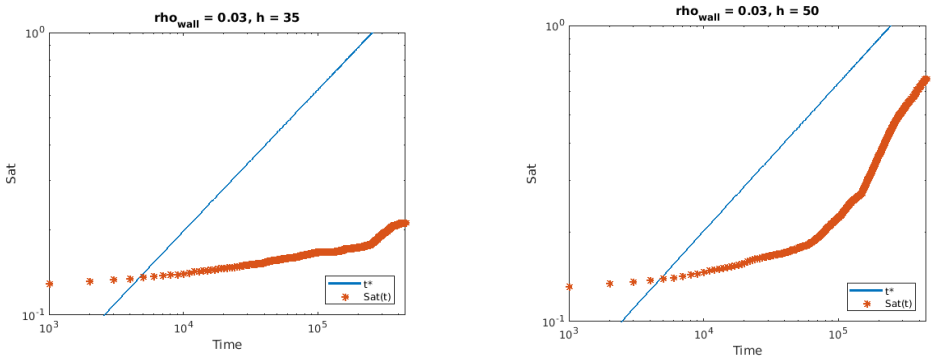

(a) Case MP 2.

(b) Case MP 6.

Figure 4.4: MP 2 and 6 extended to 450,000 iterations.

It is noteworthy to mention that when running these simulations from 150,000 to 450,000 iterations the code was updated to redefine contact angle values however the modifications are minimal therefore we consider these plots to be reasonably accurate. It is clear that increasing the hydraulic head allows for eventual imbibition after sufficient energy accumulates to break the surface tension force. This phenomenon is called a capillary barrier and more information regarding this can be found in [34] and [35]. Since we have identified problematic cases regarding imbibition when the solid mactrix is only slightly hydrophilic we wish to analyze the evolution of the liquid front over time.

4.2 Liquid front evolution over time

When looking into the liquid front evolution we will focus on a more limited number of cases, particularly of interest are the borderline blockage cases. In the interest of clarity we will relist the cases that will be considered within this section.

Table 4.2: Multiphase cases run using LBM, OC - old code, NC - new code.

Case	h	ρ_{wall}	Additional Notes
MP 1	35	0.06	OC
MP 2	35	0.03	OC+NC
MP 6	50	0.03	OC+NC
MP 8	15	0.04	NC

We plot the penetration depths of the water as a function of time and look at the effect of channeling (or ganglia formation) due to the wetting process. This physical phenomena can be described by the increased local hydraulic conductivity due to the changing contact angle in pre-wetted areas. In such areas the liquid will follow these established paths rather than create new ones. On the microsocopic scale there exists the concept of dynamic contact angles and their effect on the flow patterns in the capillary structure. This process is beyond the scope of this work however it can be noted that these effects can be considered significant in conditions with heterogeneous surface smoothness and specific flow conditions. The interested reader is invited to pursue this topic in the works of [36], [37], [38] and [39]. The presented graphs show the largest depth at which the liquid phase has penetrated by the given iteration number. They do not represent a particular 2D plane but rather a "map" of the ganglia formation as a function of the domain. If we refer to Figure 3.4 as a reference the top of the porous zone is equivalent to 0 and the bottom of the porous zone is 70 in Figures 4.5, 4.6 and 4.7.

By comparing the liquid penetration depth between the different cases we can look at the formation of ganglia or alternately determine if the flow is primarily spatially homogeneous. In Figures 4.5a, 4.6a and 4.7a we see that the pattern is relatively homoegneous, likely due to the moderately high hydrophilicity which facilitates the flow and prevents any capillary barrier formation. The other cases are less homogeneous and exhibit the formation of localized ganglia. This behaviour can be used to channel flow through porous media in specific patterns provided one can keep a desired area wetted or by finding another method to facilitate a similar effect.

It is worthwhile to discuss the penetration pattern formation at time $t = 150,000$ for two reasons. In Figure 4.7a we can see that the vast majority of the liquid has reached the base of the porous layer and the purple areas denote the location of solid particles within the matrix. In Figure 4.7d we see a slightly more homogeneous distribution that those present in 4.7b and 4.7c. This leads to the hypothesis that even a slight shift in hydrophilicity has a larger effect on flow distribution than seen by the increase in hydraulic head. It is which this consideration in mind that we

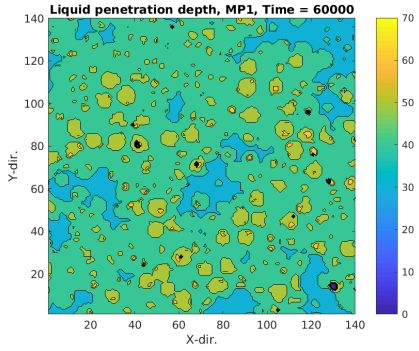

(a) Case MP 1.

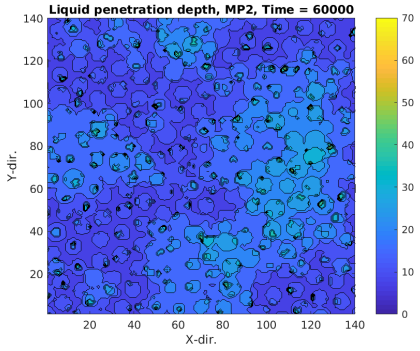

(b) Case MP 2.

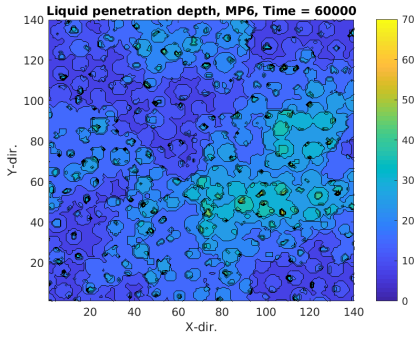

(c) Case MP 6.

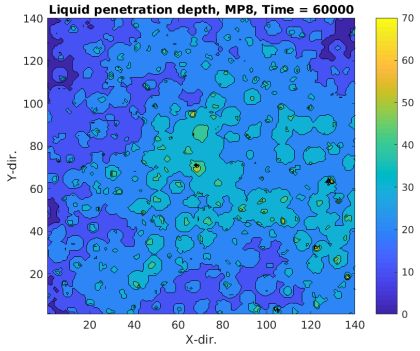

(d) Case MP 8.

Figure 4.5: Liquid penetration depth at $t = 60,000$.

continue our analysis of these cases by calculating the interfacial areas between the 3 phases present in our simulation.

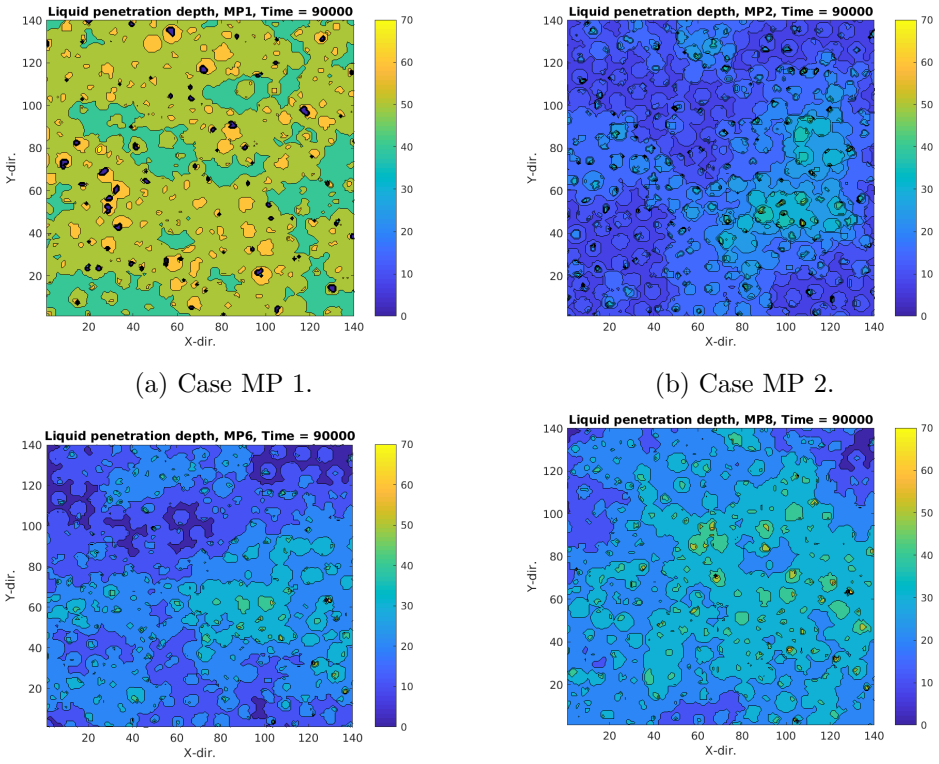

(a) Case MP 1.

(b) Case MP 2.

(c) Case MP 6.

(d) Case MP 8.

Figure 4.6: Liquid penetration depth at $t = 90,000$.

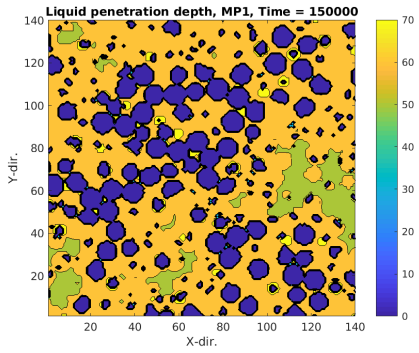

(a) Case MP 1.

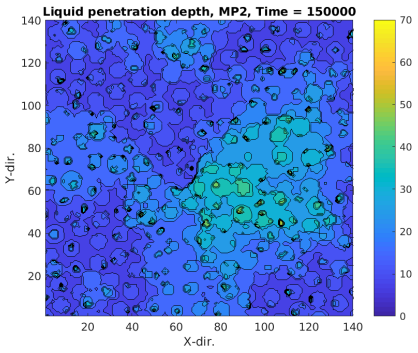

(b) Case MP 2.

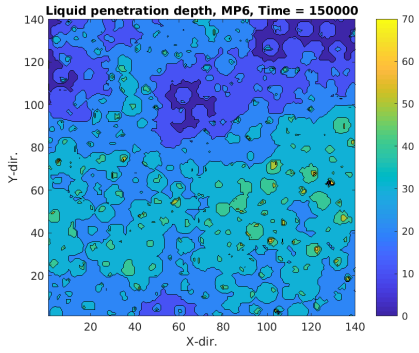

(c) Case MP 6.

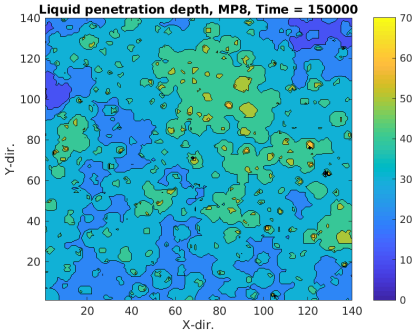

(d) Case MP 8.

Figure 4.7: Liquid penetration depth at $t = 150,000$.

4.3 Liquid-air interfacial area

In this section we will look at the effect of cumulative interfacial areas over the domain as a function of time. This information can be of use since we know that in order to facilitate faster saturation we need to maximize the liquid-solid interface. The primary obstacle to this is the balance between the gravity effect on the liquid and the interfacial surface tension. The increase in total liquid-solid interface within the domain is plotted in Figure 4.8, although we should mention that minute changes cannot be captured over the full time interval. What we can see is the direct correlation between wetted area of the solid matrix and saturation. This is unsurprising due to the definition of saturation however we cannot consider interfacial area at a given depth only due to the penetration inhomogeneity we have observed previously in section 4.2. The best method to bypass this issue is to look only at a particular time interval of interest but this is not covered in this work as we find the liquid-air interface of more interest.

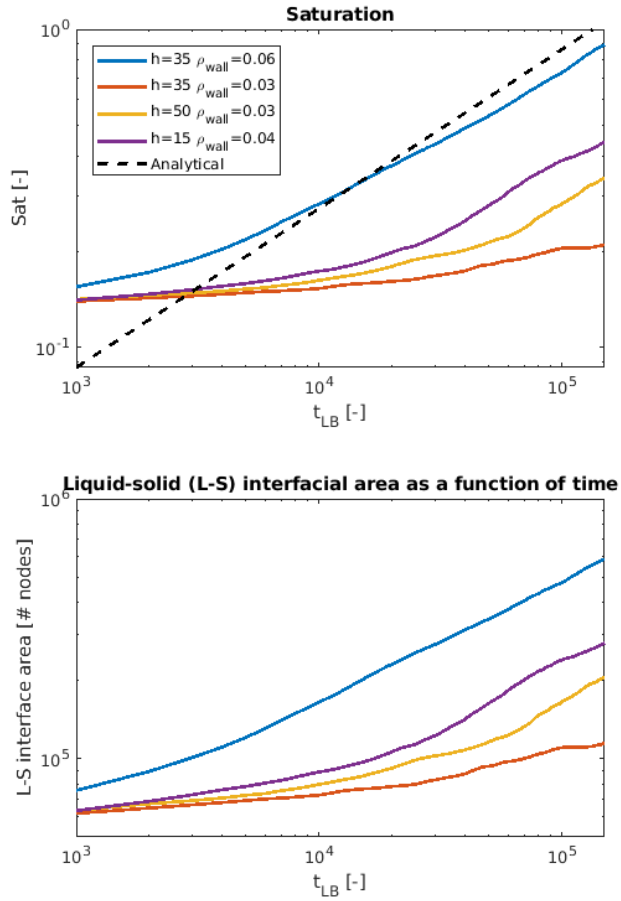

Figure 4.8: Saturation and liquid-solid interfacial area over time.

In Figure 4.9 we can see the initial buildup of liquid-air interfacial area followed by the sharp decline which loosely corresponds to the beginning of the saturation

for the case with higher hydrophilicity. The other cases are much more difficult to accurately evaluate however we can see that the slower the imbibition the lower the interfacial area seems to be. In addition, we do not see such pronounced variation as in the more active cases which may correspond to the homogeneity of flow when compared to isolated pockets of infiltration.

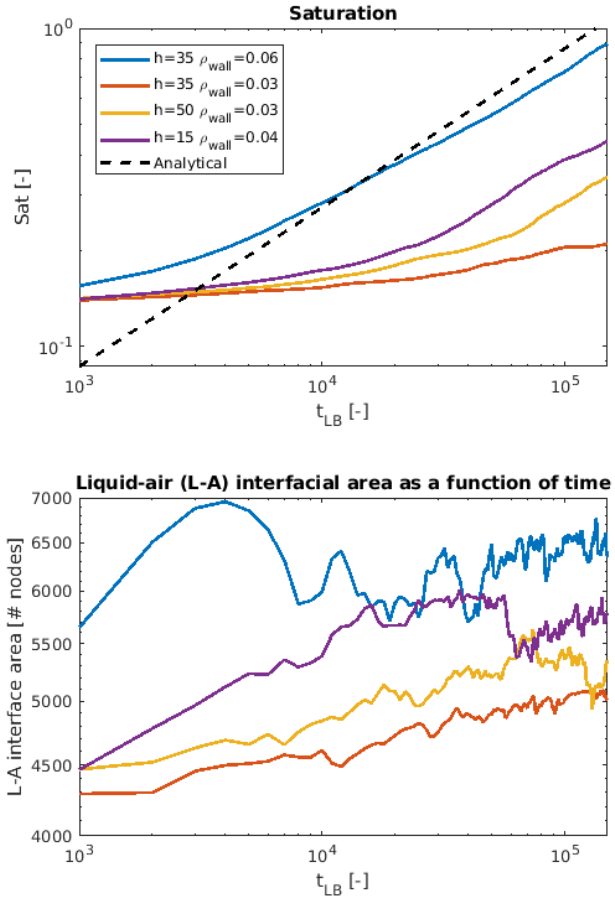

Figure 4.9: Saturation and liquid-air interfacial area over time.

When it comes to practical implications we can say a few words regarding the liquid-air interfacial area. When designing a porous structure with the intention of multiphasic flow, particularly that of decently large density differences as with air and water, it could be a good idea to look into the effects of rapidly expanding pores and their contribution to blockages in infiltration. While it is an extension to claim infiltration problems arise solely due to this phenomenon we can state that as interfacial areas increase rapidly in the flow direction we do see blocking effects. A more prduent designer may take this into account and attempt to reduce such blockage problems by introducing a more hydrophilic material or adding particles of variable radius to reduce the possibility of such pore expansions forming in a randomly packed medium. Further work must be done to accurately quantify this

effect however we believe it is worth a mention.

This concludes the results obtained thus far and so in the next chapter we provide a short conclusion and discuss future work on the mesoscopic and macroscopic level as well as experimental plans.

Chapter 5

Conclusions on LBM and future work

Up to this point we have managed to examine in relative detail the relationships between hydrophilicity of the porous matrix and the subsequent flow patterns we observe. This information is already valuable from a design perspective in that one can choose materials with specific hydrophilic/phobic properties and particle sizes to perform under specific conditions. We also get a glimpse of the methodology that can be applied to optimizing packing structures if so desired or at all possible in practical situations. It is possible to extend this investigation further with regard to pore structures and their direct influence on flow patterns or blockage.

5.1 Future plans

There are several paths on which one can continue the investigations within the topic discussed in this work, both at the meso-scale and at the macroscopic scale and both will be considered. We will begin with a small discussion on the continued application of LBM on the mesoscopic scale and what more information we can extract from such simulations that can be of use for our work.

5.1.1 Mesoscopic scale

One important thing to note that as of yet we have not performed any simulations on drainage of the porous matrix however we know from extensive literature on the topic that the imbibition and drainage processes behave differently and that the difference is known as hysteresis. It would be of value to confirm this effect on our porous matrices of choice and indeed compare the results to some experimental data if possible. The most difficult aspect of this validation would be to procure a sample for testing and accurately reproduce its lattice structure in 3D with decent accuracy. This is possible using imaging techniques however one must be careful not to disrupt porous matrix during experimentation as any cracks or shifting of material will alter the results. In addition material purity may be an issue as well as the scale at which

these experiments must be performed.

Another interesting possibility to tackle is the characterization of the porous medium itself with regard to pore structure and connection. Since we know from previous discussion that hydrophilicity plays an important role on imbibition, we can explore other parameters that we can modify to improve or tweak performance as desired. These parameters can include surface roughness, particle size characterization, layering of materials, etc. Specific designs may be possible by using these parameters whereby they facilitate imbibition from the surface but actively retard drainage for a given amount of time. The possibilities for such designs can be an attractive argument for pursuing such research and the applications are not limited to the subject matter discussed in this work.

Thermal effects should also be considered at some stage and this inclusion will alter the performance of a given porous structure, if we include the possibility of freezing especially. This topic is quite a difficult one to tackle as some work would be necessary to determine the temperature range at which the relationship between relative permeability and saturation can be charcterized by a singular function. If one desires to contruct a system that can dynamically change this relationship simply given temperature at a locality this tool can be quite powerful in hydraulic performance predictions, particularly if one also allows for dynamic changes to the lattice when freezing occurs, however this is beyond the scope of this text and will not be considered further.

5.1.2 Macroscopic scale

If we return to the macroscopic scale there are several prominent issues to be tackled to complete the proposed model and validate its applicability to green roofs. We will cover first the final step in modeling stormwater flow in green roofs and this text with a brief discussion on experimentation and plans for validation at a variety of scales.

Implementation of saturation in CFD model

We have discussed how one can generate the curves relating saturation and relative permeability that are necessary when modeling macroscopic flow through porous media. The implementation of this information can be tricky since we have calculated it for a given volume over a time interval, thus we must have a way to relate this correctly in a CFD simulation where computational cells (volumes) are not necessarily uniform across the domain. We must therefore detect the presence of liquid when it crosses into a computational cell and enforce the relationship of saturation over time and its corresponding relative permeability. This can be done by introducing custom scalar fields however this step has not been finalized as of this text and the exact method not set in stone. It is immediately evident that such an approach must be

validated thus it is in our best interest to test this proposed method against well documented cases, either from simulations and/or experimental data.

Experimental work

In addition to the finalization of the model several experiments are planned to provide comparative data that can be used to validate the model at a variety of levels. The experiments will be carried out in two stages. The first stage will be to construct a laboratory experiment to measure imbibition and drainage of a homogeneous porous material layering and compare the results to our simulations. Once this has been completed and the results are satisfactory a single green roof "tile" will be tested similarly under controlled conditions. Representative material properties will have to be extracted and used as inputs to the model. It will be of use to quantify the error when moving from a well-defined homogeneous material to the real product which includes the vegetation itself. Since we are in a controlled environment we can eliminate some sources of error and pinpoint the contributions from inhomogeneity, vegetation, etc., though to separate such contributions precisely would be a monumental task and is not of real interest to us at this stage. Finally we have access to full-scale green roof experimental results, courtesy of efforts by NTNU and SINTEF in Trondheim, Norway [40]. This data can be used to check the scalability of the simulation work proposed in this text to realistic conditions. If we are able to predict performance with reasonable accuracy at a small scale there is no guarantee this will scale to larger installations and it is imperative to analyze this possibility to deterimine the precise applicability of such simulations. This comparison will be the final step in the proposed work plan as it is the culmination of an effort that spans from modeling flow at the mesoscopic scale where interial forces are insignificant when compared to surface tension to determining performances of roofs of more than 80 square meters.

5.2 Final thoughts

It is constructive to point out that while none of the methods presented in this work are new, their combination in the methodology presented here is novel. In particular, the application of lattice Boltzmann to solve unsaturated soil aggregate behaviour for use in larger scale simulations is an approach that looks promising. If it is possible to extract accurate information on the relationship between relative permeability and saturation without peforming extensive experimentation and use the results in macroscopic simulations; we can greatly reduce the time required to solve such problems and provide a tool to optimize design performance in terms of imbibition at the mesoscopic scale.

References

[1] Inc., G. R. *Introduction to green roofing*. 2013. URL: http://godfreyroofing.com/commercial/education/roofing-articles/introduction-to-green-roofing/ (cit. on p. 3).

[2] Vijayaraghavan, K. and Joshi, U. "Application of seaweed as substrate additive in green roofs: Enhancement of water retention and sorption capacity". In: *Landscape and Urban Planning* 143 (2015), pp. 25–32. DOI: 10.1016/j.landurbplan.2015.06.006 (cit. on p. 4).

[3] Lunain, D. et al. "In-situ evaluation of the acoustic efficiency of a green wall in urban area". In: *Proceedings of the INTER-NOISE 2016 - 45th International Congress and Exposition on Noise Control Engineering: Towards a Quieter Future*. 2016, pp. 6592–6601 (cit. on p. 4).

[4] Olsson, J. et al. *Extremregn i nuvarande och framtida klimat Analyser av observationer och framtidsscenarier*. Swedish. Report, Series Klimatologi 47. SMHI. URL: https://www.smhi.se/publikationer/publikationer/extremregn-i-nuvarande-och-framtida-klimat-analyser-av-observationer-och-framtidsscenarier-1.129407 (cit. on p. 4).

[5] Stovin, V. et al. "A modelling study of long term green roof retention performance." In: *Journal of environmental management* 131 (Dec. 2013), pp. 206–215. DOI: 10.1016/j.jenvman.2013.09.026 (cit. on p. 4).

[6] Masseroni, D. and Cislaghi, A. "Green roof benefits for reducing flood risk at the catchment scale". In: *Environmental Earth Sciences* 75.7 (2016). DOI: 10.1007/s12665-016-5377-z (cit. on p. 4).

[7] Wong, G. K. L. and Jim, C. Y. "Quantitative hydrologic performance of extensive green roof under humid-tropical rainfall regime". In: *Ecological Engineering* 70 (Sept. 2014), pp. 366–378. DOI: 10.1016/j.ecoleng.2014.06.025 (cit. on p. 4).

[8] Blocken, B. and Carmeliet, J. "Spatial and temporal distribution of driving rain on a low-rise building". In: *Wind and Structures, An International Journal* 5.5 (2002), pp. 441–462. ISSN: 1226-6116. DOI: 10.12989/was.2002.5.5.441 (cit. on p. 5).

[9] Blocken, B. and Carmeliet, J. "Validation of CFD simulations of wind-driven rain on a low-rise building facade". In: *Building and Environment* 42.7 (July 2007), pp. 2530–2548. DOI: 10.1016/j.buildenv.2006.07.032 (cit. on p. 5).

[10] Kubilay, A. et al. “Numerical modeling of turbulent dispersion for wind-driven rain on building facades”. In: *Environmental Fluid Mechanics* 15.1 (June 2014), pp. 109–133. DOI: 10.1007/s10652-014-9363-2 (cit. on p. 5).

[11] Kubilay, A. et al. “Numerical simulations of wind-driven rain on an array of low-rise cubic buildings and validation by field measurements”. In: *Building and Environment* 81 (Nov. 2014), pp. 283–295. DOI: 10.1016/j.buildenv.2014.07.008 (cit. on p. 5).

[12] Abuku, M. et al. “On the validity of numerical wind-driven rain simulation on a rectangular low-rise building under various oblique winds”. In: *Building and Environment* 44 (2009), pp. 621–632. ISSN: 0360-1323. DOI: 10.1016/j.buildenv.2008.05.003 (cit. on p. 5).

[13] Blocken, B. and Carmeliet, J. “High-resolution wind-driven rain measurements on a low-rise building—experimental data for model development and model validation”. In: *Journal of Wind Engineering and Industrial Aerodynamics* 93.12 (Dec. 2005), pp. 905–928. DOI: 10.1016/j.jweia.2005.09.004 (cit. on p. 5).

[14] Kubilay, A. et al. “High-resolution field measurements of wind-driven rain on an array of low-rise cubic buildings”. In: *Building and Environment* 78 (Aug. 2014), pp. 1–13. DOI: 10.1016/j.buildenv.2014.04.004 (cit. on p. 5).

[15] Nore, K. et al. “A dataset of wind-driven rain measurements on a low-rise test building in Norway”. In: *Building and Environment* 42.5 (May 2007), pp. 2150–2165. DOI: 10.1016/j.buildenv.2006.04.003 (cit. on p. 5).

[16] Pettersson, K. et al. “Simulating wind-driven rain on building facades using Eulerian multiphase with rain phase turbulence model”. In: *Building and Environment* 106 (2016), pp. 1–9. DOI: 10.1016/j.buildenv.2016.06.012 (cit. on p. 5).

[17] Mobilia, M. et al. “Including a-priori assessment of actual evapotranspiration for green roof daily scale hydrological modelling”. In: *Water (Switzerland)* 9.2 (2017). DOI: 10.3390/w9020072 (cit. on p. 5).

[18] Johannessen, B. et al. “Detention and retention behavior of four extensive green roofs in three Nordic climate zones”. In: *Water (Switzerland)* 10.6 (2018). DOI: 10.3390/w10060671 (cit. on p. 5).

[19] Gray, W. G. “A derivation of the equations for multi-phase transport”. In: *Chemical Engineering Science* 30.2 (Feb. 1975), pp. 229–233. ISSN: 0009-2509. DOI: 10.1016/0009-2509(75)80010-8 (cit. on p. 8).

[20] Zhu, T. et al. “A Study of the Time Constant in Unsteady Porous Media Flow Using Direct Numerical Simulation”. In: *Transport in Porous Media* 104.1 (Aug. 2014), pp. 161–179. ISSN: 1573-1634. DOI: 10.1007/s11242-014-0326-3 (cit. on p. 11).

[21] Beavers, G. and Joseph, D. “Boundary conditions at a naturally permeable wall”. In: *Journal of Fluid Mechanics* 30.1 (1967), pp. 197–207. DOI: 10.1017/S0022112067001375 (cit. on p. 13).

[22] Jäger, W. and Mikelić, A. "On the interface boundary condition of Beavers, Joseph, and Saffman". In: *SIAM Journal on Applied Mathematics* 60.4 (2000), pp. 1111–1127 (cit. on p. 13).

[23] Whitaker, S. "Flow in porous media I: A theoretical derivation of Darcy's law". In: *Transport in Porous Media* 1.1 (1986), pp. 3–25. DOI: 10.1007/BF01036523 (cit. on p. 14).

[24] Brooks, R. H. et al. *Hydraulic properties of porous media*. Hydrology papers 3. Fort Collins, Colorado: Colorado State University, 1964 (cit. on p. 15).

[25] Maggiolo, D. "Numerical modeling and fluid-dynamic optimisation of fuel cells and flow batteries systems". Doctoral Thesis. Università degli Studi di Padov, 2017. URL: https://www.researchgate.net/profile/Dario_Maggiolo/publication/318745439_Numerical_Modeling_and_Fluid-Dynamic_Optimization_of_Fuel_Cells_and_Flow_Batteries_Systems/links/597b21220f7e9b0469ec7011/Numerical-Modeling-and-Fluid-Dynamic-Optimization-of-Fuel-Cells-and-Flow-Batteries-Systems.pdf (cit. on p. 17).

[26] McNamara, G. and Zanetti, G. "Use of the boltzmann equation to simulate lattice-gas automata". In: *Physical Review Letters* 61.20 (1988), pp. 2332–2335. DOI: 10.1103/PhysRevLett.61.2332 (cit. on p. 20).

[27] Higuera, F. and Jiménez, J. "Boltzmann approach to lattice gas simulations". In: *EPL* 9.7 (1989), pp. 663–668. DOI: 10.1209/0295-5075/9/7/009 (cit. on p. 20).

[28] Maggiolo, D. *A Lattice-Boltzmann open-source code project by Dario Maggiolo*. 2017. URL: https://gitlab.com/dariom/lbdm.git (cit. on p. 22).

[29] Galindo-Torres, S. et al. "Boundary effects on the Soil Water Characteristic Curves obtained from lattice Boltzmann simulations". In: *Computers and Geotechnics* 71 (2016), pp. 136–146. DOI: 10.1016/j.compgeo.2015.09.008 (cit. on p. 22).

[30] Bajare, D. et al. "Pore structure of lightweight clay aggregate incorporate with non-metallic products coming from aluminium scrap recycling industry". In: *Journal of the European Ceramic Society* 32.1 (2012), pp. 141–148. DOI: 10.1016/j.jeurceramsoc.2011.07.039 (cit. on p. 22).

[31] Glover, P. et al. "Permeability prediction from MICP and NMR data using an electrokinetic approach". In: *Geophysics* 71.4 (2006). DOI: 10.1190/1.2216930 (cit. on p. 23).

[32] Glover, P. and Walker, E. "Grain-size to effective pore-size transformation derived from electrokinetic theory". In: *Geophysics* 74.1 (2009). DOI: 10.1190/1.3033217 (cit. on p. 23).

[33] Boccardo, G. et al. "Validation of a novel open-source work-flow for the simulation of packed-bed reactors". In: *Chemical Engineering Journal* 279 (2015), pp. 809–820–820. DOI: 10.1016/j.cej.2015.05.032 (cit. on p. 23).

[34] Ferrari, A. et al. “Challenges in modeling unstable two-phase flow experiments in porous micromodels”. In: *Water Resources Research* 51.3 (2015), pp. 1381–1400. DOI: 10.1002/2014WR016384 (cit. on p. 32).

[35] Ross, B. “The diversion capacity of capillary barriers”. In: *Water Resources Research* 26.10 (1990), pp. 2625–2629. DOI: 10.1029/WR026i010p02625 (cit. on p. 32).

[36] Hazlett, R. and Vaidya, R. “Lattice Boltzmann simulations and contact angle hysteresis in convergent-divergent media”. In: *Journal of Petroleum Science and Engineering* 33.1-3 (2002), pp. 161–171. DOI: 10.1016/S0920-4105(01)00183-8 (cit. on p. 33).

[37] Latva-Kokko, M. and Rothman, D. “Static contact angle in lattice Boltzmann models of immiscible fluids”. In: *Physical Review E - Statistical, Nonlinear, and Soft Matter Physics* 72.4 (2005). DOI: 10.1103/PhysRevE.72.046701 (cit. on p. 33).

[38] Benzi, R. et al. “Mesoscopic modeling of a two-phase flow in the presence of boundaries: The contact angle”. In: *Physical Review E - Statistical, Nonlinear, and Soft Matter Physics* 74.2 (2006). DOI: 10.1103/PhysRevE.74.021509 (cit. on p. 33).

[39] Huang, H. et al. “Proposed approximation for contact angles in Shan-and-Chen-type multicomponent multiphase lattice Boltzmann models”. In: *Physical Review E - Statistical, Nonlinear, and Soft Matter Physics* 76.6 (2007). DOI: 10.1103/PhysRevE.76.066701 (cit. on p. 33).

[40] Hamouz, V. et al. “Hydrological performance of LECA-based roofs in cold climates”. In: *Water (Switzerland)* 10.3 (2018). DOI: 10.3390/w10030263 (cit. on p. 43).

Part II

Appended papers

Paper 1

Simulating wind-driven rain on buildings facades using Eulerian multiphase with rain phase turbulence model.

Pettersson Kaj, Krajnovic Sinisa, Sasic Kalagasidis Angela and Johansson Pär

Building and Environment 106 (2016), pp. 1–9.

https://doi.org/10.1016/j.buildenv.2016.06.012